*Journal of Metamorphic Geology*

WILEY

Journal of METAMORPHIC GEOLOGY

ORIGINAL ARTICLE OPEN ACCESS

# Interplay Between Mechanical and Petrochemical Models on the Fluid Extraction From Subduction Zones

Thorsten Andreas Markmann[1] | Pierre Lanari[1,2]

[1]Institute of Geological Sciences, University of Bern, Bern, Switzerland | [2]Institute of Earth Sciences, University of Lausanne, Lausanne, Switzerland

**Correspondence:** Thorsten Andreas Markmann (thorsten.markmann@unibe.ch)

**Received:** 17 July 2024 | **Revised:** 25 September 2025 | **Accepted:** 2 October 2025

**Funding:** This project has received funding from the European Research Council (ERC) under the European Union's Horizon 2020 research.

**Keywords:** brittle failure | fluid fluxes | permeability | software solution | thermodynamic modelling | ThorPT

## ABSTRACT

The breakdown of hydrous minerals during subduction results in a densification of the rocks, producing volume changes that can trigger fluid pressure fluctuations and hydrofracturing. These volume changes are controlled by the Clapeyron slope of the reaction and are quantified here using a macroscopic framework that integrates a zero-dimensional mechanical model and a one-dimensional petrological model. A Mohr–Coulomb–based mechanical model is coupled with phase equilibrium calculations (Theriak-Domino), oxygen isotope fractionation and trace element partitioning, using the compressed compensated Redlich–Kwong (CORK) equation of state to describe fluid properties. This model can predict fluid pressure fluctuations and brittle-failure events from successive Gibbs free energy minimisations while accounting for tensile strength and differential stress in the mechanical model. The code is released as an open-source Python library ThorPT. For intermediate subduction geotherms, results indicate up to 5 vol.% fluid-filled porosity without brittle failure, consistent with findings from several geophysical studies. In basalts and serpentinites, the calculated time-averaged permeability values show intermittent episodes of permeability exceeding $10^{-19}$ m$^2$. In serpentinite, the permeability increase can be attributed to olivine formation. In mafic rocks, episodes of increased permeability are associated with the breakdown of chlorite, amphibole and lawsonite during the transition from blueschist to eclogite. In the case of warm subduction geotherms, the model results show a strong correlation between dehydration-driven brittle failure, fluid migration and seismicity, particularly in the mafic crust. The blueschist–eclogite transition is associated with intense brittle failure, matching geothermal and geophysical models linking this depth range to seismic double layers. Our results highlight the coupled mechanism of dehydration reaction and brittle failure as a driver of episodic fluid extraction, with broad implications for fluid–rock interaction and mass transfer in subduction zones.

## 1 | Introduction

There are several metamorphic reactions occurring in the Earth's crust and mantle that consume or produce aqueous fluids consisting of $H_2O$ with amounts of $CO_2$, $CH_4$ and other aqueous species. In subduction zones, these fluids contribute significantly to arc magmatism, mass transfer and seismicity (Bebout and Penniston-Dorland 2016; Etheridge et al. 2021; Hacker, Abers, and Peacock 2003; Kerrick and Connolly 2001; Kirby et al. 1996; Padrón-Navarta, Tommasi, et al. 2010; Peacock 2009; Saffer and Tobin 2011; Sibson 2013). During prograde metamorphism, the $H_2O$ bound in minerals is released as the minerals break down, contributing to the production of aqueous fluids. Released fluids can migrate vertically upward within rock grain boundaries, fractures or other structural patterns, as they are volatile and less dense than the solids (Ague 2014; Malvoisin et al. 2015). Brittle deformation in the crust has often been associated with fluid

production during metamorphic reactions and fluid migration away from the production site (Cox 2010; Etheridge 1983; Giuntoli et al. 2024; Gold and Soter 1984; Hacker, Peacock, et al. 2003). The movement of a fluid along grain boundaries is referred to as pervasive flow, whereas channelled flow occurs along highly permeable domains (Ague 2014; Zack and John 2007). There is evidence that dehydration can lead to both fluid channelling and pervasive fluid migration (Bovay et al. 2021; Huber et al. 2022; Stewart and Ague 2020; Zack and John 2007).

Two main approaches have been used in previous studies to gain a better understanding of fluid production and fluid flow in the crust.

- Global fluid fluxes have been investigated using petrological and/or petrochemical models. Both models rely on phase equilibrium modelling, the prediction of mineral stability and phase transformation using Gibbs free energy minimisation. Such one-dimensional models in the *P–T* space are macroscopic. The system is defined using a bulk rock composition with internal microstructures or compositional variations at the microscale not being considered (Lanari and Engi 2017). Petrological models simulate how the mineral assemblage of a given rock system changes with changing pressure and temperature conditions and can estimate the magnitude of fluid fluxes (e.g., Baxter and Caddick 2013; Konrad-Schmolke et al. 2005, 2006; Konrad-Schmolke, O'Brien, et al. 2008). For example, garnet growth—often associated with a dehydration reaction—can be linked to water production during progressive burial in the subduction zone (Baxter and Caddick 2013). Petrochemical models extend the petrological models by incorporating isotope geochemistry such as oxygen isotope fractionation or trace element partitioning (Kohn 1993; Vho et al. 2020; Konrad-Schmolke, Zack, et al. 2008). These models have been instrumental in studying fluid–rock interaction processes, particularly in explaining the fluid-induced trace element patterns commonly observed in high-pressure minerals. Additionally, they allow for the simulation of oxygen isotopic compositions in stable mineral and fluid phases under both closed- and open-system conditions (Vho et al. 2020). The extension to multi-layer models enables the simulation of fluid production in specific lithologies, such as serpentinites, and its infiltration into other lithologies, including mafic or metasedimentary layers, while also tracking the resulting changes in the isotopic signatures of bulk and mineral phases. Similarly, these simulations can be applied to model water transfer from the subducting slab into the forearc mantle wedge, leading to serpentinisation (Vho et al. 2020). Applying fluid transfer models to large-scale scenarios such as subduction zones can quantify not only the fluid fluxes associated to dehydration reactions but also the amount of deeply subducted water that is recycled to the deep mantle (Gies et al. 2024). However, these models do not take into account the possible mechanical mechanisms that control fluid extraction, which is assumed either to be instantaneous or to occur when the amount of fluid exceed a threshold value (Wilson et al. 2014).
- The second approach is to use thermomechanical models that can simulate fluid movement in porous media. These two-phase flow models involve porous compaction and viscous–plastic deformation of the solid matrix, mass and momentum conservation coupled with Darcy flow for the fluid (Connolly 1997; Malvoisin et al. 2015; McKenzie 1984; Morishige and van Keken 2018; Wang et al. 2019). Mass, momentum and energy conservative equations are solved to describe the fluid or melt movement by compaction. Different matrices and geological problems can be tested by using such an approach; for example, the transport velocity of major and trace elements in melt could be estimated (McKenzie 1984). A similar approach can also be applied to rocks that undergo devolatilisation reactions. This approach would result in an aqueous fluid pressure gradient, and the reaction front propagation can be described as a creep of porosity waves (Connolly 1997). The fluid pathways in a dehydrating subducting slab have been simulated using this approach, confirming the possibility of trenchward or arcward fluid movements (Morishige and van Keken 2018; Wang et al. 2019). Typically, such 2D or 3D simulations are designed for kilometre-scale models and rarely consider mineral reactions as predicted by thermodynamic models. Models that include deformation mechanisms rely on permeability and fluid viscosity, parameters that are still poorly constrained (McKenzie 1984; Morishige and van Keken 2018; Wilson et al. 2014). Coupling thermodynamic data with such models often involves trade-offs. It must neglect deformation, assume specific fluid flow conditions (e.g., buoyancy-driven movement) or rely on static, precomputed thermodynamic data—such as look-up tables or fluid production budgets of different lithologies based on their reaction progress—for acceptable performance (Malvoisin et al. 2015). In addition, mineralogical and chemical reactions can affect viscous flow and estimated fluid release in subduction zone models, which in turn modify permeability and fluid migration (Beinlich et al. 2020; Bras et al. 2023; Plümper et al. 2012). These models allow reactions, fluid release and permeability development to be investigated on a microscopic scale. Plümper, John, et al. (2017) also showed that fluid flow in dehydrating rocks does not necessarily follow a Darcy behaviour. Dehydration reactions are associated with the nucleation and growth of minerals and can often be described by a reaction front propagating in a network.

Geophysical studies point out the increase in the P-to-S velocity ratio, attributed to the reduced shear resistance compared to compressional resistance in fluid-bearing rocks, which is interpreted to reflect zones of high fluid-filled porosity of up to 4 vol.% (Abers et al. 2009; Audet et al. 2009; Egbert et al. 2022; Gosselin et al. 2020; Kodaira et al. 2004; Peacock 2009; Peacock et al. 2011; Shiina et al. 2013). Controversially, the presence of free fluid in the crust is often associated with extensional hydraulic fracturing or shear failure (Bukała et al. 2020; Cox 2010; Cox et al. 1987; Etheridge 1983; Etheridge et al. 1983; Jung et al. 2004; Niu et al. 2003; Secor 1965; Sibson 2017; Sippl et al. 2018). Furthermore, field and microstructural observations in serpentinites, which act as direct witnesses to fluid transfer and intermediate-depth seismicity,

indicate brittle fracturing and shearing by vein structures associated with serpentinite dehydration (Muñoz-Montecinos et al. 2024; Ulrich et al. 2024). To date, hydration and dehydration reactions associated with positive and negative volume changes have been simulated using the phase field method or the distinct element method (Schmalholz et al. 2023; Evans et al. 2020; Okamoto and Shimizu 2015; Okamoto et al. 2017; Jamtveit et al. 2008) to study reaction-induced fracturing in rocks at the microscale. This has allowed the coupling of a hydraulic-mechanical response with chemical processes. These models link specific fluid production reactions to a mechanical model but neglect the reaction complexity of natural systems, which is reasonably well captured by phase equilibrium models (Hernández-Uribe and Palin 2019). The volume changes predicted by phase equilibrium models can be linked to the mechanical failure of rocks, and a first attempt has been proposed for melts but is limited to isobaric conditions (Etheridge et al. 2021).

In this study, we propose a framework for petrochemical modelling that combines chemical equilibrium calculations and isotope fractionation with a mechanical model of brittle rock failure. The implementation in Python is distributed as an open-source modelling package ThorPT available at https://github.com/neoscalc/ThorPT. The thermodynamic calculations are performed using Theriak-Domino (de Capitani and Brown 1987; De Capitani and Petrakakis 2010) combined with an oxygen isotope fractionation model (Vho et al. 2020) and a trace element distribution model (Konrad-Schmolke et al. 2023; Konrad-Schmolke, Zack, et al. 2008). Mechanical failure is predicted using a mechanical model based on the Mohr–Coulomb theory. Fluid extraction from the system is assumed to occur when brittle failure occurs and is also compared to a threshold extraction method. This combined model is applied to different rock types to re-evaluate fluid extraction during the subduction of altered oceanic crust and to investigate possible triggers.

## 2 | Mechanical Model for Rock Failure and Fluid Extraction

### 2.1 | Failure Criteria

The occurrence and mechanisms of brittle deformation in rocks buried below the brittle–ductile transition are a standing debate in geology (e.g., Yamato et al. 2019). In classical rock mechanics, brittle rock failure is described semi-quantitatively as a function of material properties (internal friction, tensile strength and cohesion) and the applied differential stress (Jaeger et al. 2007; Sibson 2013 and references therein). This framework allows rock integrity to be assessed at the scale of a single material point, i.e., in a zero-dimensional sense. The failure envelope in normal stress–shear stress space is defined as

$$\tau = C + \left(\sigma_n - P_f\right) \cdot \mu, \tag{1}$$

where $\tau$ is the shear stress (MPa), $\sigma_n$ is the normal stress and $P_f$ is the fluid pressure with the material properties $C$ for the rock cohesion (MPa) and $\mu$ the internal friction coefficient (see Figure 1a). In this space, the stress state of the rock is represented by a circle, with a diameter equal to the differential stress. The differential stress can be obtained from the maximum and minimum normal stresses:

$$\Delta\sigma = \sigma_1 - \sigma_3. \tag{2}$$

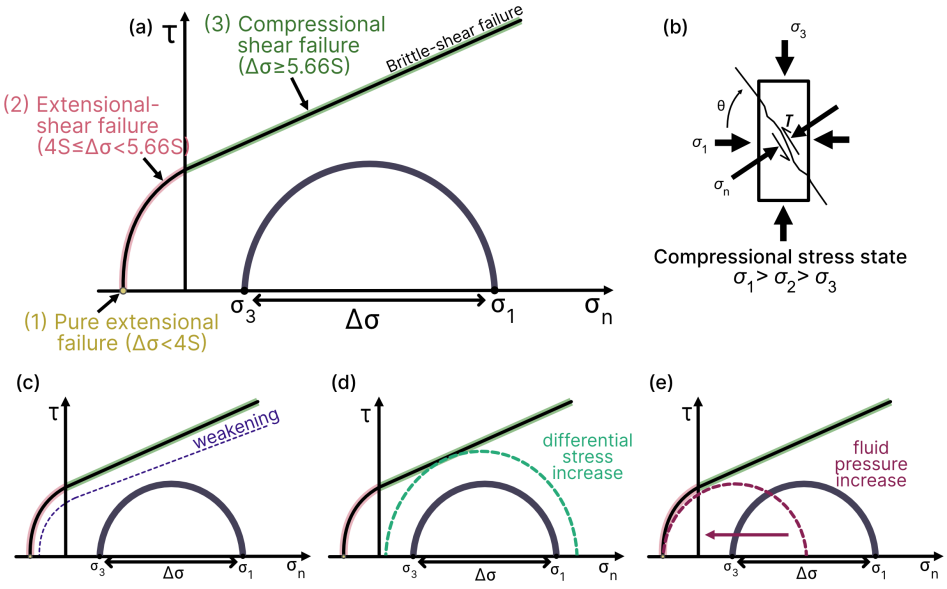


**FIGURE 1** | Mohr–Coulomb failure mode diagram in compressive stress state. (a) Representation of the rock as a circle in the shear stress-normal stress space and the failure envelope. The diameter of the circle is defined by the differential stress (see Equation 3). Failure modes can be (1) pure extension failure (yellow), (2) extension-shear failure (red) and (3) compression-shear failure (green). (b) Compression stress state of the rock system showing maximum, minimum and normal stress and the angle of misorientation of the failure plane. (c) Weakening of the rock by changing $S$ and $\mu$ results in a displacement of the failure envelope (modified after Yamato et al. 2019). (d) Increasing the shear stress changes the differential stress and therefore the circle diameter. (e) An increase in fluid pressure drives the circle toward a lower normal stress.

The Griffith failure criterion is an extension of the Mohr–Coulomb failure criterion describing failure for tensile normal stress:

$$\tau^2 = 4S^2 + 4S(\sigma_n - P_f), \tag{3}$$

where $S$ is the tensile strength of the rock (MPa) and follows the empirical observation with the cohesion $C \approx 2 \cdot S$ (see Figure 1; Griffits 1921; Jaeger et al. 2007; Secor 1965; Sibson 2000).

In a rock without fluid, failure can occur only due to changes in the material properties ($\mu$, $C$ or $S$; see Figure 1c) or by an increase in the shear stress on the system (Figure 1d). In a rock system including fluid, the fluid pressure applies a mechanical effect and acts as an additional tensile stress on the rock system (Figure 1e). The normal stress is reduced by the amount of the fluid pressure to an effective stress $\sigma'$ (e.g., Secor 1965) defined as follows:

$$\sigma_1' = \sigma_1 - P_f, \quad \sigma_3' = \sigma_3 - P_f, \text{and } \sigma_n' = \sigma_n - P_f. \tag{4}$$

This rock mechanics framework allows the failure of a rock to be evaluated in three different ways (Figure 1a).

1. **Pure extensional failure** as the brittle extensional failure, also known as hydraulic fracturing or Mode 1 cracks, requires low differential stress expressed by the condition $\Delta\sigma < 4 \cdot S$ and the minimum effective normal stress to overcome the tensile strength of the rock. The critical fluid pressure is defined as follows:

$$P_f^{crit} = \sigma_3 + S. \tag{5}$$

2. **Extensional-shear failure** applies for intermediate differential stress values with the condition $\Delta\sigma < 4 \cdot S < 5.66 \cdot S$. The critical fluid pressure is defined as (Cox 2010) follows:

$$P_f^{crit} = \frac{8\,S\,(\sigma_1 + \sigma_3) - (\sigma_1 - \sigma_3)^2}{16\,S}. \tag{6}$$

3. **Compressional shear failure** occurs for high differential stress values with $\Delta\sigma \geq 5.66 \cdot S$, resulting in a critical fluid pressure defined as follows:

$$P_f^{crit} = \frac{C}{\mu} + \frac{\sigma_1 + \sigma_3}{2} - \frac{\sigma_1 - \sigma_3}{2}\cos(2\theta) - \frac{\sigma_1 - \sigma_3}{2\mu}\sin(2\theta), \tag{7}$$

where $\theta$ is the misorientation angle corresponding to the angle between a fault and the maximum normal stress $\sigma_1$ (Cox 2010).

## 2.2 | Coupling Thermodynamic Modelling With Failure Mechanics

Thermodynamic models can be used to simulate the evolution of a rock system along a pressure–temperature path (e.g., Baxter and Caddick 2013; Hernández-Uribe and Palin 2019; Lanari and Duesterhoeft 2019). These petrological models assume a closed system that is in thermodynamic equilibrium, as predicted by Gibbs free energy minimisation. They can be combined into petrochemical models by incorporating calculations of oxygen isotope or trace element fractionation for the stable mineral assemblage (e.g., Konrad-Schmolke, Zack, et al. et al. 2008; Konrad-Schmolke et al. 2011; Vho et al. 2020). Coupling these petrochemical models with failure mechanics requires a framework to link thermodynamic pressure with the differential stress, fluid pressure and volume changes from mineral reactions.

In classic equilibrium thermodynamics, a closed system at fixed pressure ($P$) and temperature ($T$) conditions evolves toward equilibrium by minimising its Gibbs free energy (e.g., Brown and Skinner 1974; de Capitani and Brown 1987). The system can be composed of solid mineral phases and fluid phases (Figure 2). For simplicity, only an aqueous fluid is considered as the dominant fluid phase in the following. The thermodynamic pressure of such a closed system is the same for all mineral phases and for the fluid, which is a requirement for thermodynamic equilibrium (e.g., Lanari and Duesterhoeft 2019). At equilibrium, i.e., when the Gibbs free energy is minimised, the system has relaxed to any differential stress and represents a static system under thermodynamic pressure (Moulas et al. 2019; Nordstrom and Munoz 1994). Moulas et al. (2019) demonstrated that the mean stress of a system is close to the lithostatic pressure $P_{lith}$ over large timescales (> 10 kyr) including changes in volume and differential stress values lower than 100 MPa. In this case, the lithostatic pressure $P_{lith}$ can be used as the thermodynamic pressure $P$ for modelling. Nevertheless, there is currently no widely accepted consensus in the literature on how to include anisotropic stress in thermodynamics. This means that any model combining the two relies on assumptions (Wheeler 2020; Hobbs and Ord 2018; Powell et al. 2018; Tajčmanová et al. 2015). Following Moulas et al. (2019), in a system with a fluid-filled porosity, the fluid pressure is close to the lithostatic pressure, representing the mean stress (see Figure 2; Connolly and Podladchikov 2004; Etheridge et al. 2021; Hobbs and Ord 2018; Saffer and Tobin 2011; Sibson 2013).

In a system represented by a container, let us assume that a small amount of fluid is present in association with the solids and that the fluid is in mechanical equilibrium with the solids. At this scale, microstructural and textural relationships are neglected and the system is treated macroscopically. At thermodynamic equilibrium, the fluid pressure is equal to the thermodynamic pressure. As $P$–$T$ conditions change, the volumes of the phases in this container may also change, which can be calculated using the bulk system composition and Gibbs energy minimisation for each $P$–$T$ condition. In such a re-equilibrating system, the Clausius-Clapeyron relation expresses the change in volume and entropy of the products of a reaction associated with a change in pressure and temperature. As an example, a typical fluid-producing reaction involving the formation of garnet in a system with a basaltic composition (Baxter and Caddick 2013) is examined below. At the initial conditions of 0.85 GPa and 375°C, the system consists of solid phases with an initial assemblage of clinopyroxene, chlorite, white mica, glaucophane, zoisite, titanite and quartz ($Asm_{start}$). The system

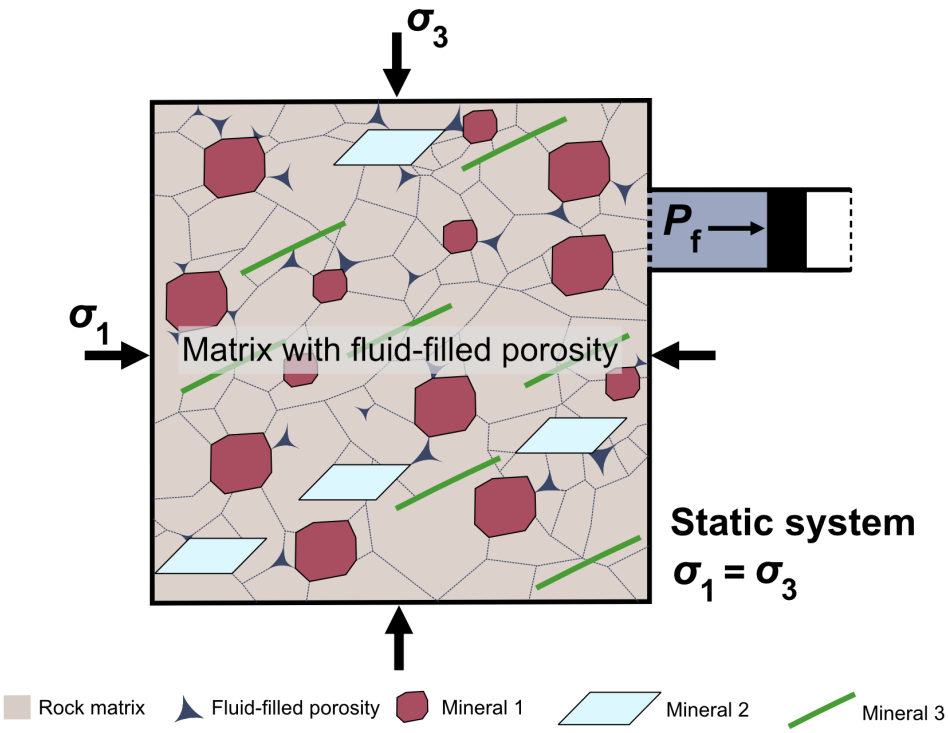


**FIGURE 2** | Visualisation of a hypothetical section through a rock system consisting of mineral porphyroblasts in a mineral matrix and a fluid-filled porosity, which is connected in 3D. The system is assumed to be closed and at thermodynamic equilibrium therefore there has no differential stress ($\sigma_1 = \sigma_3$). The fluid pressure can be modified from the surrounding and is represented by a valve mechanism (modified after Hobbs and Ord 2018). When the system receives pressure changes from internal work (volumetric changes) and/or surrounding (increasing vertical load or shear stress) the fluid pressure will adapt to the new condition by moving the valve mechanism. The variables $\sigma_1$ and $\sigma_3$ represent the maximum and minimum normal stress, respectively and $P_f$ is the fluid pressure. Note that when the fluid volume changes the fluid pressure should change accordingly as indicated by the black arrow at the valve. It should be noted that the microscopic representation of the process is for illustrative purposes only and that the models discussed in the text are macroscopic.

is then re-equilibrated to form garnet and fluid at six different *P*–*T* conditions, corresponding to six different Clapeyron slopes (see Figure 3). The re-equilibrated system is then represented by $Asm_1$. The temperature increment is constant while the pressure changes for each simulation. Depending on the Clapeyron slope defined by *P*/*T*, the total volume of the system will either increase or decrease (Figure 3). Assemblages with a larger pressure increase (steeper Clapeyron slope) can cause a total volume decrease of up to 4.6% and those with a smaller pressure increase (less steep Clapeyron slope) can cause a total volume increase of up to 2.4%.

As discussed above, macroscopic phase-equilibrium modelling based on thermodynamics and the minimisation of Gibbs free energy can be used to predict how the total volume of a rock system with a known bulk composition evolves under varying *P*–*T* conditions. When the same bulk composition is used at different *P*–*T* conditions, the model simulates the re-equilibration of a closed, mass-conservative system. While these calculations yield phase volumes from a thermodynamic perspective, the sum of the re-equilibrated phase volumes may differ from the original 'container' volume (Figure 2). A similar approach has been applied to melt generation in metapelite (Etheridge et al. 2021). The macroscopic model developed herein consists of two stages: a thermodynamic stage, based on Gibbs free energy minimisation to predict the rock system and a subsequent mechanical stage, in which volume changes are assessed independently of thermodynamic constraints. In a system containing fluid and given that solids are far less compressible than fluids, any mismatch between the container volume and the re-equilibrated solid volume must be accommodated by a transient change in fluid volume. If the fluid mass remains constant, its density must adjust accordingly, leading to a transient shift in fluid pressure. This transient process can be visualised with a valve–piston mechanism (Figure 2): a net decrease in the solid–fluid system volume lowers fluid pressure and moves the piston inward, whereas an expansion compresses the fluid and raises its pressure (black arrow in Figure 2). In both cases, the fluid density adapts to the new volume, controlling the pressure response to the metamorphic reaction. This model assumes that reaction kinetics are much faster than deformation, an assumption that is subject to debate (e.g., Hobbs et al. 2010; Moulas et al. 2022; Plümper et al. 2022). However, it has also been recently demonstrated that metamorphic reactions can occur very quickly (Liu et al. 2025). Accordingly, our proposed macroscopic framework assumes that reaction kinetics are faster than deformation rates. Although alternative approaches could be used to couple thermodynamic modelling with two-dimensional simulations in order to resolve microtextures and mineral–fluid interactions (Plümper, John, et al. 2017; Huber et al. 2022), these methods focus on local processes, in which reaction kinetics are more important than thermodynamic equilibrium. Lastly, the problem could be formulated using

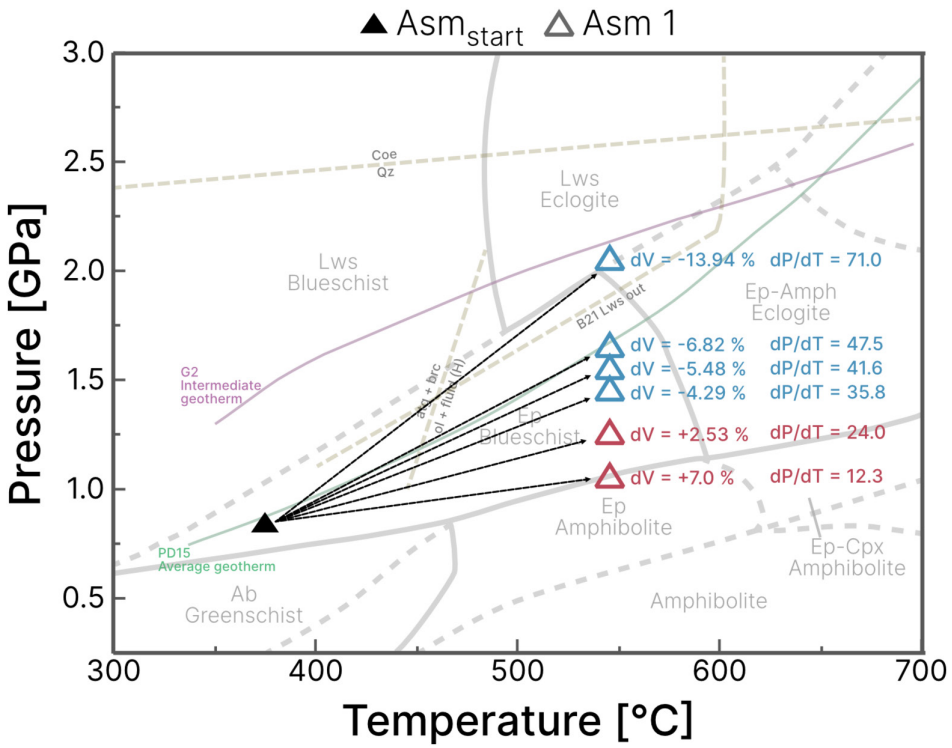


**FIGURE 3** | Volume change simulated for a mafic rock system under different increasing pressure and temperature conditions representing possible geothermal gradients in subduction zones. The violet line represents the intermediate geotherm from Gerya et al. (2002) (G2), while the green line represents the average geotherm from Penniston-Dorland et al. (2015) (PD15). Metamorphic facies are from Forshaw et al. (2024), and serpentine breakdown reactions are from Hermann et al. (2000) (H) and Padrón-Navarta, Hermann, et al. (2010) (P). Mineral abbreviations follow Warr (2021). Clapeyron slope values are reported in MPa/°C.

Helmholtz energy minimisation (under fixed $T$ and $V_{system}$) instead of Gibbs energy minimisation (under fixed $T$ and $P$), but this development is beyond the scope of this paper. The assumption that we can calculate how the total volume of solids changes with $P$–$T$ using Gibbs energy minimisation allows us to derive a simplified relationship between available pore space, fluid volume and fluid pressure.

The pressure–volume relationship of an ideal gas can be expressed by the Boyle–Mariotte law:

$$P_1 V_1 = P_2 V_2. \tag{8}$$

$P_1$ is the thermodynamic pressure (gas pressure) and $V_1$ is the volume of the gas at the $P_1$ and $T_1$ conditions. The volume $V_2$ and pressure $P_2$ describe the pressure–volume relationship for an ideal gas when $P$ or $V$ has changed.

For now, let us assume an ideal behaviour of the fluid in equilibrium with Asm$_1$. The volume of fluid $V_{fluid}$ corresponding to $V_1$ at $P_1$ predicted by equilibrium thermodynamics is compressed to a new volume $V_2$ corresponding to the total volume of the container $V_{reference}$ minus the volume of the solids $V_{solids}$. The fluid pressure $P_2$ can be calculated as follows:

$$P_2 = P_1 \frac{V_1}{V_2} = P_1 \frac{V_{fluid}}{V_{reference} - V_{solid}}. \tag{9}$$

The ratio $P_2/P_1$ represents the (pore) fluid factor (Etheridge et al. 2021 and references therein). The difference $V_{reference}$ minus $V_{solid}$ represents the available 'void' space of the reaction accessible for $V_{fluid}$.

Pressure–Volume relationships of metamorphic fluids are different from those of ideal gases, especially at high pressures. The behaviour of a metamorphic fluid at high pressures can be calculated using the Compensated-Redlich-Kwong (CORK) equation (Holland and Powell 1991). The pressure–volume relationship of the fluid is

$$P = \frac{RT}{V_m - b} - \frac{a}{V_m(V_m + b)\sqrt{T}}, \tag{10}$$

where $V_m$ is the molar volume of the fluid, $R$ is the gas constant, $T$ is the temperature, $a$ is the temperature dependent attraction term and $b$ is the covolume term (Halbach and Chatterjee 1982). The change in pressure due to volume change can be expressed using the fluid factor $P_2/P_1$:

$$\frac{P_2}{P_1} = \frac{\frac{RT}{V_{m,2} - b} - \frac{a}{V_{m,2}(V_{m,2} + b)\sqrt{T}}}{\frac{RT}{V_{m,1} - b} - \frac{a}{V_{m,1}(V_{m,1} + b)\sqrt{T}}}, \tag{11}$$

where $V_{m,2}$ is the molar volume of the compressed fluid after the dehydration reaction has occurred, which corresponds to

$$V_{m,2} = \frac{V_2}{V_1} V_{m,1.} \quad (12)$$

The compressibility of the solids is not taken into account here because the solids are much less compressible than the fluid (Holland and Powell 1996; Holland and Powell 1998; Berman 1988). In a petrological modelling framework, the Gibbs free energy can be minimised after each $P$ and $T$ increment. The change in fluid pressure can be calculated by multiplying the fluid factor from Equation (11) and the thermodynamic pressure. The fluid factor is determined from the volumes obtained after equilibration, which already include the production or consumption of fluid. After re-equilibration, volume changes are evaluated and an external differential stress can be applied to the system (see below).

Treating the system as a container and calculating the fluid pressure based solely on internal volume changes overlooks the possibility that some volume change may be absorbed by the movement of the surrounding rock material. In this case, the system can be modelled as a deformable container, where the reaction-induced void space decreases as fluid is produced after re-equilibration. In this case, $V_{\text{reference}} - V_{\text{solid}}$ can be smaller than in the case, resulting in a higher fluid pressure. This scenario can be simulated in a fluid-filled porous system, where the fluid adjusts to pressure changes caused by solid volume variations and differential stress (Mazzucchelli et al. 2024). Therefore an external differential stress parameter was introduced into the mechanical model. This parameter considers the fluid-induced weakening in the Mohr–Coulomb model (see Figure 1) and can increase the failure sensitivity of the mechanical model. However, for simplicity, the thermodynamic model does not consider differential stress and the lithostatic pressure is used instead. This assumption is reasonable for low differential stress values of less than 100 MPa (Moulas et al. 2019). In step 1, the system is in chemical and mechanical equilibrium at given $P$ and $T$ conditions (Figure 4a,b). Stage 2 represents the system after a small change in $P$ and $T$ in the absence of mechanical failure. After the reaction, the stable phases predicted by Gibbs free energy minimisation at $P_2$–$T_2$ include a fluid phase (Figure 4c). At this stage, the associated volume changes cause an increase in fluid pressure that is not sufficient to cause mechanical failure (Figure 4d). The differential stress is also not large enough to cause failure. Step 3 represents the system following a new small increment in $P$ and $T$. In this case, the associated volume change causes a further increase in the fluid pressure triggering mechanical failure (Figure 4f) causing all of the fluid to be extracted from the system (Figure 4e). The mechanical failure in this example occurs by extensional failure, but other modes are possible (see Figure 1). Step 4 represents the system after fluid extraction when it has chemically and mechanically equilibrated to $P_3$ and $T_3$ conditions (Figures 4g,h). Here, the system has relaxed after reaction and has attained a new total volume.

## 3 | Petrochemical Model Calculator ThorPT

Petrochemical modelling was performed using an open source package written in Python called ThorPT available at https://github.com/neoscalc/ThorPT. Theriak-Domino (de Capitani and Brown 1987; De Capitani and Petrakakis 2010) was used to perform the Gibbs energy minimisations for a given bulk system composition during its evolution along a $P$–$T$ path. For each iteration step, the starting rock is modelled using Gibbs free energy minimisation, giving predicted stable phase assemblages. Mineral phase fractionation is included as this effect can significantly affect the predictions of the thermodynamic model (e.g., Lanari and Engi 2017). Here, the produced garnet is fractionated at each step and a new reactive bulk composition is calculated. This approach is necessary because neglecting garnet fractionation has been shown to directly influence the proportions and compositions of other predicted phases, as well as the garnet-to-water production ratio (Baxter and Caddick 2013). Additionally, spherical diffusion for garnet major elements can be applied to account for any diffusional transport by using the Julia package 'DiffusionGarnet' (Dominguez et al. 2026). The oxygen isotope composition $\delta^{18}O$ for the predicted stable phases is modelled based on oxygen isotope fractionation (Vho et al. 2020) using an internally consistent oxygen isotope fractionation database (Vho et al. 2019). Trace element distribution between the mineral phases and the fluid is modelled using the approach and distribution coefficients of Konrad-Schmolke et al. (2023). The oxygen and trace element models are included in the model output by default but are not discussed here. Fluid extraction is implemented and can modify the reactive bulk composition for the amount of $H_2O$, the amount of $^{18}O$ and by the amount of partitioned trace elements into the fluid. Fluid extraction is regulated by the mechanical model and all of the fluid is extracted when brittle failure is predicted (see above). Further, a minimum fluid-filled porosity of 0.2 vol.% is implemented in the model, which has to be overcome to enable fluid pressure calculation. This simulates a threshold for pore space and possible interconnectivity based on studies on grain boundary wetting (e.g., Wark et al. 2003; Yoshino et al. 2006).

The user can set the following model parameters (see Table 1): (1) the $P$–$T$ path, (2) enable or disable fluid transmission and interaction, allowing or preventing the transfer of extracted fluid from one rock unit into the overlying units, (3) the thermodynamic database used for Gibbs free energy minimisation, (4) the bulk rock composition (in wt.%), (5) the number of moles of hydrogen, extra oxygen for Fe speciation and/or carbon, (6) the initial $\delta^{18}O$ value and REE compositions of the bulk rock and (7) the mechanical properties of the system including the tensile strength, differential stress and internal friction parameter. In addition, the fluid extraction scheme can be set as: (1) no extraction, (2) continuous extraction where extraction is performed at each increment when a free fluid is present or (3) discontinuous extraction occurring when brittle failure is predicted by the mechanical failure model.

### 3.1 | Pressure–Temperature Path Definition

The $P$–$T$ trajectory can be defined using the built-in Pathfinder module. This module can generate $P$–$T$–$t$ trajectories for burial or exhumation by entering a velocity and angle of movement. An existing $P$–$T$ path can be interactively digitised from an image. Here, by default, the 'subduction zone' scenario is used, generating the $P$–$T$ path for a subducting rock, which is buried below overlying lithologies simplified as a two-layer structure. The subducting slab itself can be manually defined as a column

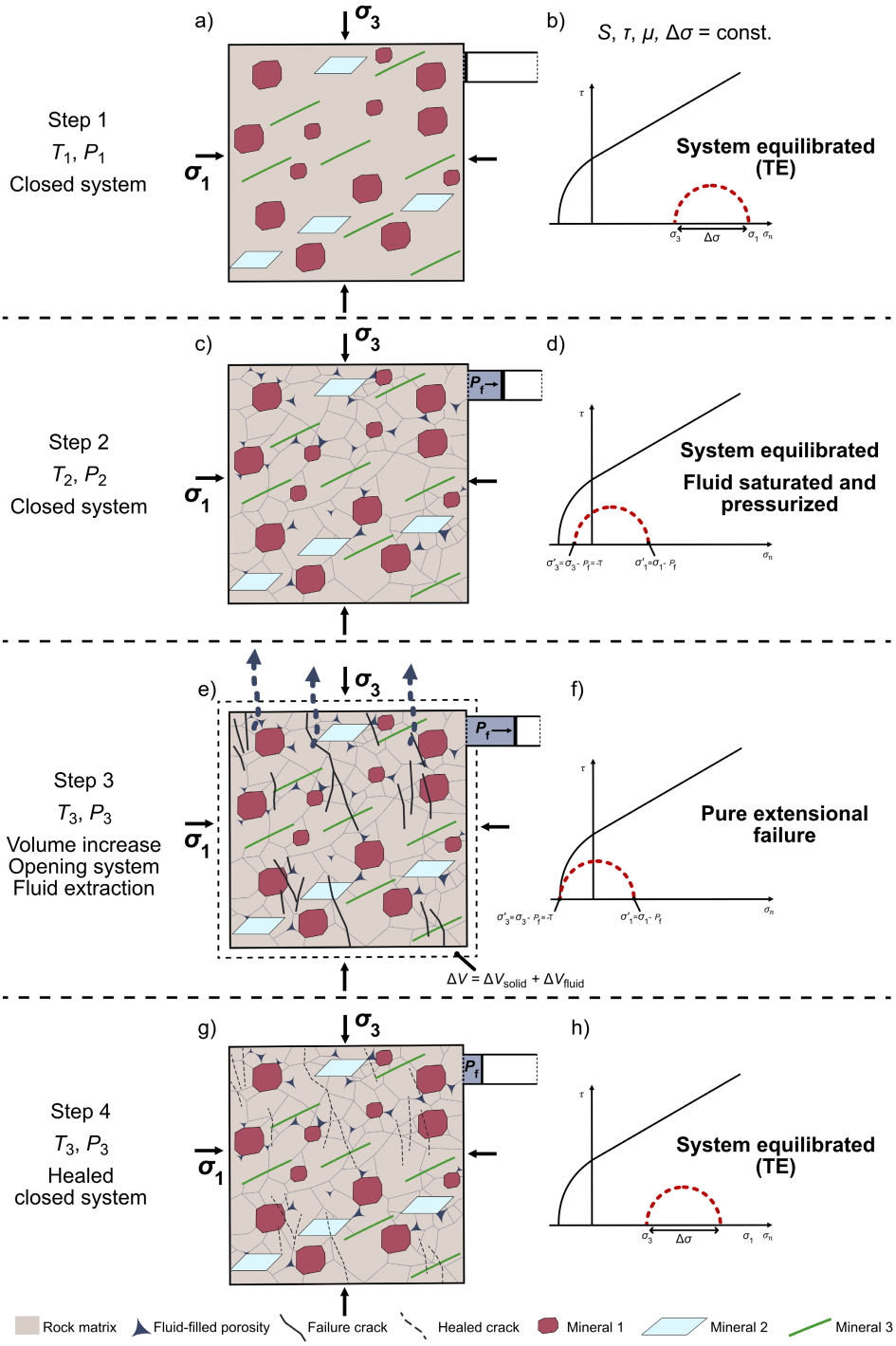


**FIGURE 4** | Failure criterion test in a system under stress and changing its solid and fluid volume during metamorphic reaction for given conditions for variables $S$, $\tau$, $\mu$ and $\Delta\sigma$. (a) Equilibrated rock system with no free fluid phase at $T_1$ and $P_1$. (b) Mohr–Coulomb diagram for the intact system. (c) Equilibrated and fluid saturated rock system at $T_1$ and $P_1$. (d) Mohr–Coulomb diagram for the intact system with fluid-filled porosity. (e) Volume change of the reacting system at the new conditions of $T_2$ and $P_2$. The system experiences a negative volume change and the fluid pressure is affecting the mechanical stability of the system (see panel d). Positive volume change and the effect on the fluid pressure is similarly calculated following Equation (11). (f) Mohr circle is moving to the left due to the change in effective stress caused by the fluid pressure and hits the failure envelope. Here, $P_f > \sigma_3$ and $\sigma'_3 \geq -S$ so that pure extensional failure is predicted. (g) After extraction, the system is healing and is in thermodynamic and mechanical equilibrium. (h) Mohr–Coulomb diagram of the healed and intact system at the new equilibrated $P$ and $T$ condition. It should be noted that the microscopic representation of the process is for illustrative purposes only and that the models discussed in the text are macroscopic. The abbreviation 'TE' indicates thermodynamic equilibrium.

of several layers in which the pressure and temperature conditions vary from top to bottom. For details, see the Supporting Information.

The path increment values in $P$ and $T$ represent the step size between two minimisations (Table 1). These values are adjustable and represent the conditions under which the reactive part of

**TABLE 1** | Overview of model set-up parameters. Selected settings represent the model used for the metabasalt benchmark.

| Description | Example rock<br>Value and comment |
|---|---|
| Type | Metabasalt (unaltered basalt after Gale et al. 2013) |
| Path increments | 500 MPa and 10°C |
| Model scenario | Isolated mode (optional: transmitting) |
| **Thermodynamic parameters** | |
| Database | tc55 (revised version of Holland and Powell 1998 and following to Vho et al. 2020) |
| Solution models | Holland and Powell (2003) for calcite–dolomite– magnesite<br>Holland and Powell (1998) for garnet, white mica and talc<br>Holland and Powell (1996) for omphacite<br>Holland et al. (1998) for chlorite<br>Diener et al. (2007) for amphibole |
| Equation of state for fluid | CORK equations from Holland and Powell (1991) |

| Oxide wt.% | $SiO_2$ | $TiO_2$ | $Al_2O_3$ | FeO | $Fe_2O_3$ | MnO | MgO | CaO | $Na_2O$ | $K_2O$ |
|---|---|---|---|---|---|---|---|---|---|---|
| Starting bulk | 50.47 | 1.68 | 14.70 | 10.43 | 0.00 | 0.00 | 7.58 | 11.39 | 2.79 | 0.16 |

| REE µg/g | La | Ce | Pr | Nd | Sm | Eu | Gd | Tb | Dy | Ho | Er | Tm | Yb | Lu |
|---|---|---|---|---|---|---|---|---|---|---|---|---|---|---|
| Start composition | 5.80 | 16.40 | 2.80 | 14.50 | 4.40 | 1.05 | 4.57 | 0.71 | 4.49 | 0.98 | 2.86 | 0.45 | 2.71 | 0.41 |

| | |
|---|---|
| Moles of hydrogen | 0.6 (Fluid saturated at the first calculation) |
| Moles of excess carbon | 0 |
| **Geochemical parameters** | |
| Oxygen isotope fractionation factors | DBOXYGEN 2.0.3 (Vho et al. 2019) |
| Starting bulk $\delta^{18}O$ | 5.7‰ |
| **Fluid and mechanical parameters** | |
| Fluid phase fractionated | water.fluid (named as in the thermodynamic database) |
| Fluid extraction mechanism | Mechanical model (optional: No extraction/continuous) |
| Fluid fraction leaving the system | 100% when present as a free fluid phase |
| Fluid pressure | Mean stress |

(Continues)

**TABLE 1** | (Continued)

| Description | Example rock<br>Value and comment |
|---|---|
| Fluid volume threshold | 100 vol.% (automatic release when value is overcome, 100 = disabled) |
| Fluid connectivity | 0.2 vol.% (minimum value to enable fluid pressure calculation) |
| Tensile strength | 20 MPa |
| Differential stress | 0 MPa |

the system reaches a new equilibrium state. Between two steps, the mineral assemblage and the fluid are held metastable without any reaction. Larger increment values may represent a delay in the reactivity of the system and can be seen as an analogue of reaction overstepping (Pattison et al. 2011; Yamato et al. 2022). In this model, a fixed incremental step size along the path was chosen based on multiple studies indicating that metamorphic reactions often require some degree of departure from rock-wide equilibrium (e.g., Carlson et al. 2015; Waters and Lovegrove 2002; Schwarz et al. 2011; Spear and Pattison 2017; Castro and Spear 2016; Pattison and Tinkham 2009). The magnitude of temperature overstepping ranges between 5°C and 90°C for different mineral reactions, with lower values typically associated with devolatilisation reactions (Carlson et al. 2015; Pattison et al. 2011). Pressure overstepping can span several hundred megapascals and for this study increment values of 500 MPa for $\Delta P$ and 10°C for $\Delta T$ were applied, assuming that reactions taking place during prograde metamorphism have relatively low energetic barriers (Rubie 1986; Waters and Lovegrove 2002; Pattison and Tinkham 2009). The temperature increment is relatively small compared to the pressure step, as mineralogical changes are often more sensitive to temperature than pressure (e.g., Rubie 1986; Ferry and Gerdes 1998; Putnis 2015; Nerone et al. 2023). Such incremental changes in temperature and pressure have been linked to garnet modal zoning associated with growth and dissolution processes (Viete et al. 2018). Once the temperature and pressure step condition is met along the predefined *P–T* path, a new Gibbs free energy minimisation is performed. The implications of modifying the step size are discussed below.

### 3.2 | Mechanical Properties

The implemented mechanical model framework depends on three parameters: the coefficient of internal friction ($\mu$), tensile strength ($S$) of the bulk rock material and the differential stress ($\Delta\sigma$) of the surrounding rock. The internal friction coefficient is set to 0.75 as a representative value for most lithologies of the crust at greater depth (Byerlee 1978; Jaeger et al. 2007; Sibson 2000). Different values of tensile strength and differential stress were tested in the mechanical model, as outlined in Section 4 and in the sensitivity analysis (Supporting Information). A summary of geological constraints on tensile strength and differential stress is provided in the Supporting Information.

## 4 | Results

### 4.1 | Comparative Test of the Combined Petrochemical Model

A comparative test of ThorPT was performed using the same model settings as in Vho et al. (2020) with an unaltered basalt bulk rock composition from Gale et al. (2013) to simulate the evolution of a metabasalt. The Gibbs free energy minimisations were performed using the internally consistent dataset of Holland and Powell (1998) with subsequent updates collected in the Theriak-Domino database tc55 (Table 1, Data S1 and S4 and Vho et al. 2020). The *P–T* trajectory was set to an oceanic subduction geotherm using a convergence speed of 0.02 m/year, a dipping angle of 20° and the path increment values were fixed at 500 MPa and 10°C (Gerya et al. 2002; see Figure S3). No differential stress was applied in this test to identify the response of the mechanical model to only fluid production and volume changes. Detailed information on the data used for input and the calculations used in the model can be found in Data S1 and S2 and Table 1.

The main simulation results are summarised in Figure 5 using mode box diagrams showing the evolution of the predicted mineral modes and the volume of fluid extracted from the system (both expressed in vol.%) along the *P–T* trajectory. The first model, shown in Figure 5a, assumes continuous fluid extraction, as described by Vho et al. (2020). In this model, fluid is continuously extracted over a series of *P–T* increments without interruption, driven by the onset of a dehydration reaction and the production of a free fluid phase. In contrast, the second model (Figure 5b) incorporates the integrated mechanical model where fluid extraction is driven by mechanical failure. This approach can result in episodic (i.e., at specific modelling steps) extraction, where fluid production and extraction occur over one or more *P–T* increments. These episodes can be interrupted by periods during which the fluid is kept in the system. The full set of results, including the simulated oxygen isotope values for the bulk rock, the fluid and the mineral phases, is given in the Supporting Information.

For both models, lawsonite, glaucophane and actinolite make up ~80 vol.% of the system at conditions below 450°C, and most of the fluid is released during garnet and omphacite

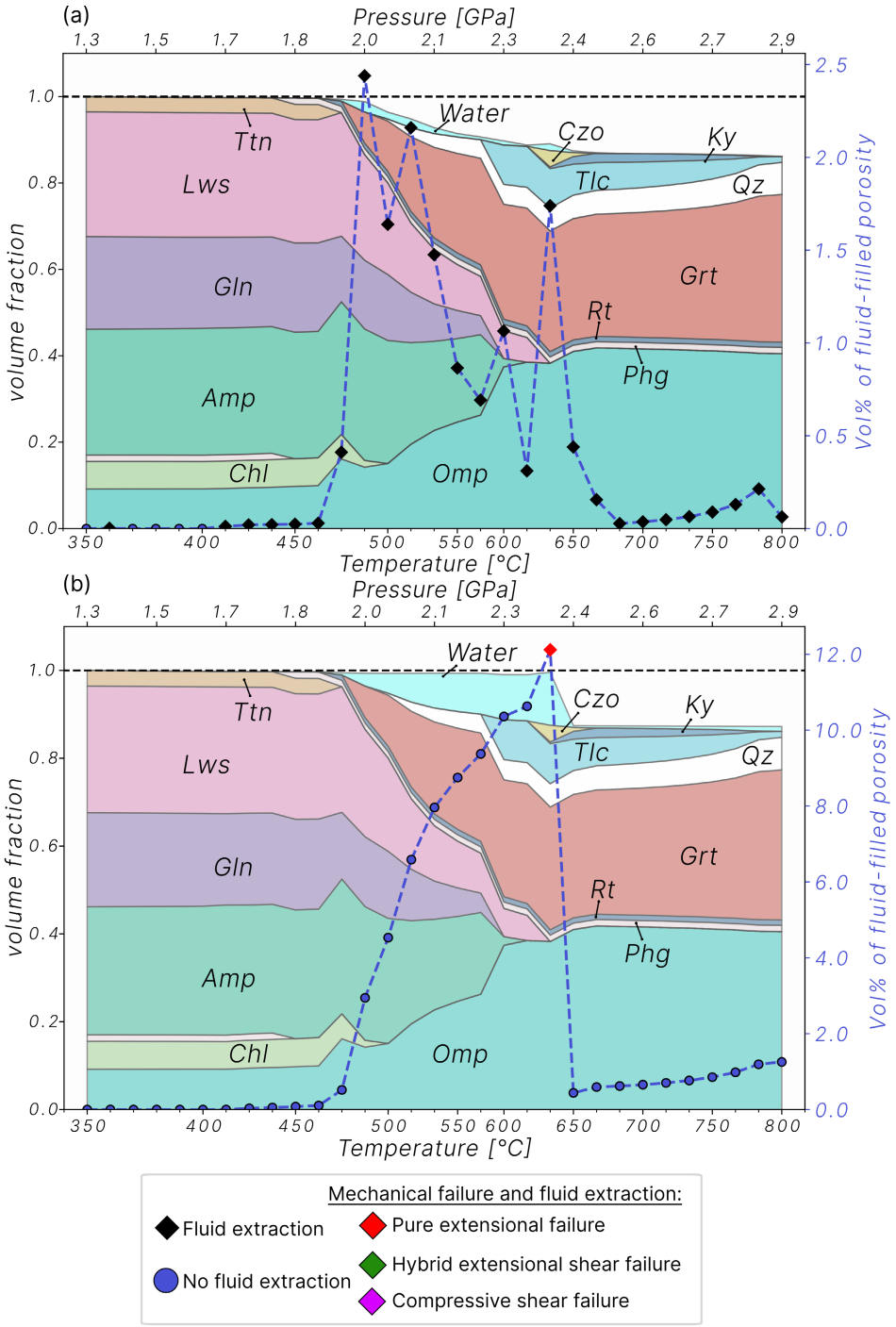


**FIGURE 5** | Box mode diagrams of an unaltered metabasalt with similar model parameters as Vho et al. (2020). Both plots show the relative volume fraction to the initial rock system on the y-axis and temperature (also increasing pressure) steps on the x-axis. The volume of fluid free fluid (in vol.% of the total system) is shown as a dashed blue line on the right y-axis with each point representing a model step. (a) Continuous extraction: the free fluid phase is always fractionated when present in the system. Each blue point indicates the amount of fluid extracted (b) Fluid extraction associated with mechanical failure: the free fluid phase is fractionated only when failure is predicted by the mechanical model. Mineral abbreviations are after Warr (2021).

growth associated with chlorite, amphibole and lawsonite breakdown. This reproduces the results of Vho et al. (2020). In both models, the main dehydration occurs between 450°C and 650°C. The first model predicts continuous fluid production and extraction at each increment, whereas the second model indicates a single discrete fluid extraction event at ~640°C and 2.36 GPa, following a period of fluid accumulation within a fluid-filled porosity. At ~650°C, both models predict a similar cumulative extracted fluid volume of ~12 vol.%. In the absence of external fluid infiltration, the predicted mineral phases in both models have similar oxygen isotope signatures (see Figure S2-2).

### 4.2 | Fluid Extraction Behaviour

The fluid extraction episodes predicted by the mechanical model were examined using the *P*–*T* path representing the geotherm of the previous model based on the *P*–*T* path of (Gerya et al. 2002; see Figure 3). Two rock types were studied, a metabasalt (unaltered basalt composition from Gale et al. [2013]) and a serpentinite (bulk rock composition from Ulrich et al. [2024]). The thermodynamic models used the internally consistent dataset of Holland and Powell (1998) and the tc55 and tc55_Serp databases, similar to Vho et al. (2020) and Kempf et al. (2020) (see the Supporting Information for details). For the mechanical model, the serpentinite is assumed to have a low competence ($S = 3$ MPa), while the metabasalt is assumed to have a high competence ($S = 20$ MPa). Simulations were performed for a range of differential stress values ranging from 0 to 500 MPa for the metabasalt and from 0 to 50 MPa for the serpentinites. However, differential stresses exceeding ~100 MPa are beyond the upper limit recommended by Moulas et al. (2019). Results above this threshold are therefore shown only for sensitivity testing and are not used in the main interpretation. Details of each model are given in Data S1. Figure 6a,b shows the mode box plots for both lithologies using a differential stress of 50 MPa for both rock types, which is an average value taken from the compilation in Figure 4b.

The metabasalt simulation predicts two distinct episodes of fluid extraction, both associated with pure extensional failure (red diamonds in Figure 6a). Prior to the first episode, which begins at ~510°C, the breakdown of chlorite, amphiboles and lawsonite produces ~6 vol.% of fluid-filled porosity. At ~510°C, the mechanical model predicts pure extensional failure allowing fluid to be extracted from the system. This episode is associated with chlorite breakdown, garnet and quartz growth. Subsequent mechanical failures continue during ongoing fluid production from amphiboles and lawsonite to ~575°C, forming a series of failure

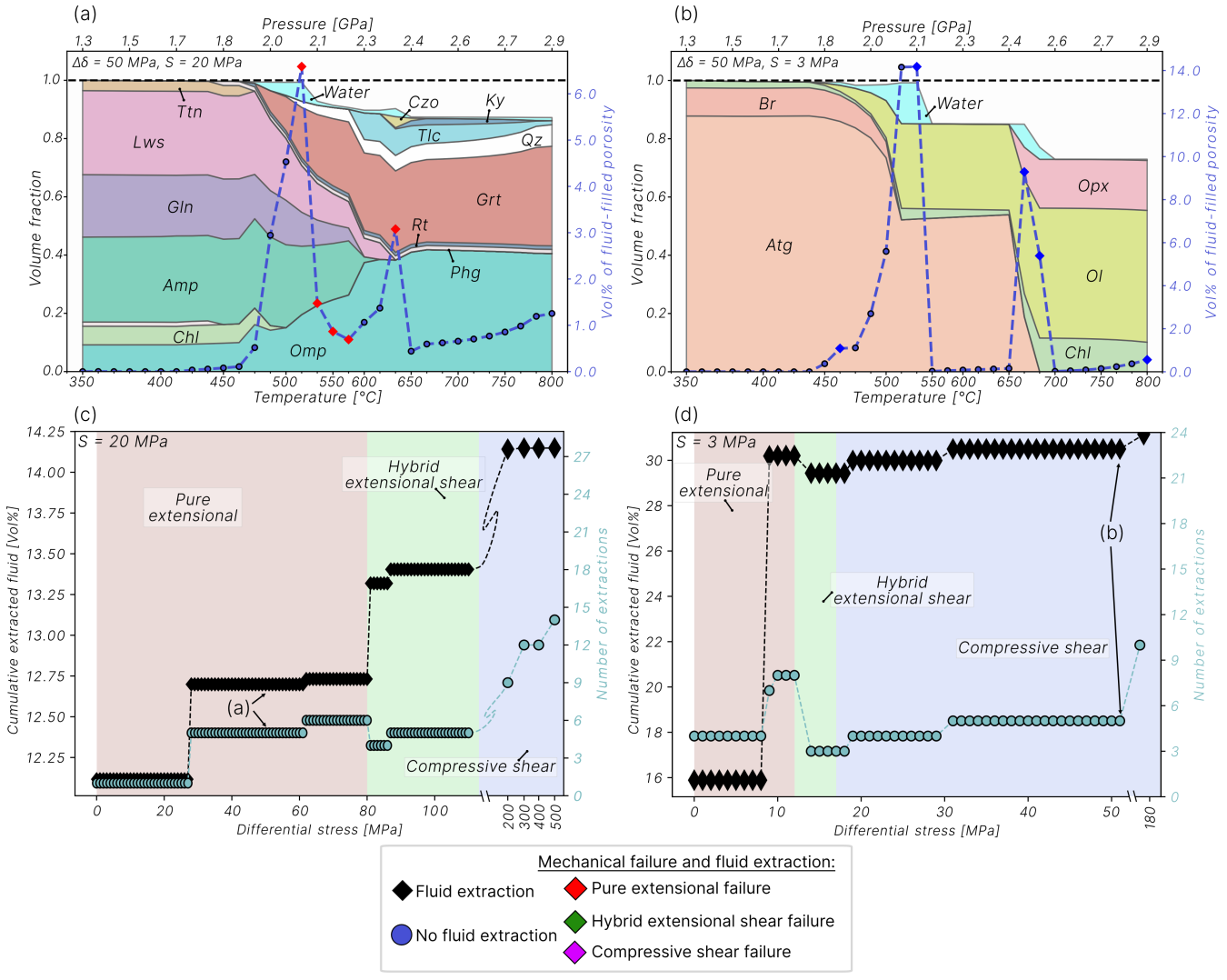


**FIGURE 6** | Modelling of metabasalt and serpentinite systems for a range of differential stress values. (a-b) Mode box diagram of the metabasalt and serpentinite with the evolution of the fluid-filled porosity (dashed blue line). Diamond marker show the type of mechanical failure and episodes of fluid extraction from the system. (c-d) Cumulative fluid volume extracted from the system and number of fluid extraction steps vs. values of differential stress. Domains of failure mode are colour coded for pure extensional failure (red), extensional shear failure (green) and compressive shear failure (blue). The used differential stress of 50 MPa in model of (a) and (b) are annotated in (c) and (d), respectively. See text for modelling details. Mineral abbreviations are after Warr (2021).

events and fluid release episodes. After this period, no further failure episode is predicted and fluid-filled porosity begins to accumulate due to the continued dehydration of amphiboles and lawsonite. At ~575°C, a second failure episode is predicted, coinciding with the disappearance of lawsonite and the formation of zoisite. This episode, also involving pure extensional failure, results in the extraction of ~3 vol.% of fluid. Following this episode, only minor amounts of fluid (~1 vol.%) are generated as pressure and temperature continue to increase.

In the serpentinite simulation, four distinct episodes of mechanical failure and fluid extraction are predicted, all associated with compressive shear failure (Figure 6b). The first major release occurs at ~460°C during the consumption of chlorite, the dehydration of brucite and antigorite and formation of olivine. This episode is responsible for the extraction of ~1 vol.% fluid. After this episode, fluid production increases, reaching several volume percent per modelling step. Once brucite is completely consumed, compressive shear failure is predicted and a large fluid amount of ~14 vol.% is extracted in a single episode. Subsequently, chlorite continues to break down, producing fluid and stabilising additional antigorite. Antigorite breaks down at ~670°C, forming chlorite, orthopyroxene and olivine. This process initiates a series of compressive shear failures, responsible for the extraction of ~10 and 5 vol.% of fluid over a 50°C interval. At the end at ~800°C, the model predicts a last failure episode associated with pure compressive shear and is linked to the dehydration of chlorite.

### 4.3 | Sensitivity of the Mechanical Model

The sensitivity of the model to differential stress was tested for the metabasalt and the serpentinite. The results are shown in Figures 7c,d with an addition in Figure S2-3. A tensile strength value of 20 MPa was taken for the rocks at various differential stress values. The same *P*–*T* path of Gerya et al. (2002) was used for the simulations. All modelling details are summarised in the Supporting Information.

For the metabasalt, an increase in differential stress leads to more extraction steps if the differential stress remains below 4*S* (≤ 80 MPa), which corresponds to the pure extensional failure domain (Figure 6c). At zero differential stress, a single fluid extraction event is predicted, as shown in the mode box diagram (Figure 5b). As the differential stress increases beyond 27 MPa, the number of extraction steps increases to five, resulting in a cumulative increase in fluid extraction from ~12.10 vol.% to ~12.70 vol.% . Within the pure extensional domain, the highest cumulative fluid extraction (~12.75 vol.%) occurs at 80 MPa and involves six extraction steps. Beyond this threshold, in the hybrid extensional-shear domain, the extraction pattern shifts (Figure S2-3), resulting in fewer extraction steps (4–5) but a larger cumulative fluid volume of up to ~13.4 vol.% . When testing very high differential stress values above 5.66 S (> 113 MPa), representing compressive shear failure, the model predicts the highest fluid release (~14.2 vol.%) with up to 14 extraction steps (Figure S2-3b). However, at such high stresses, the assumption that lithostatic pressure equals mean stress is no longer valid. These values are therefore presented only for sensitivity testing and are not included in our main model analysis.

The sensitivity test for the serpentinite simulation indicates that the mechanical model predicts brittle extensional failure at low differential stress values below 4*S* (< 12 MPa). Within this pure extensional domain, fluid extraction ranges from 16 vol.% to 30 vol.%, corresponding to 4 to 8 extraction events, respectively (Figure 6d). The upper limit of 30 vol.% is close to the maximum amount of fluid that can be extracted (see Figure S2-3c for comparison). For differential stress increases between 4*S* (12 MPa) and 5.66*S* (17 MPa), the model predicts a transition to hybrid extensional-shear failure. In this domain, the number of extraction events decreases to three, with a cumulative fluid extraction of approximately 29 vol.% (Figure S2-3d). At differential stresses above 17 MPa, the system enters the compressive shear failure domain, where the number of extraction events increases to five, resulting in a maximum cumulative fluid extraction of ~31 vol.%.

The sensitivity of fluid extraction to tensile strength and bulk rock composition is summarised in the Supporting Information. Simulations of tensile strength variations were performed for the metabasalt model (Figure S2-4). In addition, bulk rock composition sensitivity tests included the standard metabasalt composition, the average metabasalt from Winter (2014) and the bulk compositions from Belgrano and Diamond (2019). For these tests, a 20 MPa tensile strength was applied to rocks under varying differential stress conditions. Details and modelling parameters are given in the Supporting Information, specifically Figure S2-5. Overall, an increase in tensile strength of 10 MPa shifts the onset of the same failure pattern by 20 MPa. Meanwhile, modifications to basaltic composition result in a lower cumulative extracted fluid volume. The lowest fluid extraction values were observed in the bulk rock composition with the lowest $K_2O$ and highest FeO content compared to both the average and primary basalt compositions.

## 5 | Discussion

In the combined model implemented in ThorPT, fluid extraction is restricted when brittle failure occurs, i.e., during hydrofracturing, and it is assumed that 100% of the fluid present in the fluid-filled porosity is extracted. However, significant fluid migration in rocks is only feasible if the porosity and permeability are sufficiently high, such as in reaction-induced nanopores (Plümper, Botan, et al. 2017) or interconnected fluid networks along the grain boundaries (Wark et al. 2003; Yoshino et al. 2006). Generally, experimental and analytical results show that fracturing represents a rapid enhancement of the permeability in a rock by crack growth and surface enlargement (Nguyen et al. 2020; Sun et al. 2015). Cracks and fractures serve as flow channels representing conduits of high permeability (Ague 2011; Norton and Knapp 1977; Gold and Soter 1984). Regions of high fluid flow can be recorded by features such as crack-seal veins (Ramsay 1980) or allow the drainage of the fluid from the rock system (Peacock 2009). These fluid releases can then be followed by earthquakes (Viete et al. 2018).

The ThorPT petrochemical model is further evaluated below, starting with the calculation method for volume changes. Key model parameters are then examined, including those of the mechanical model, the magnitude of pressure and temperature

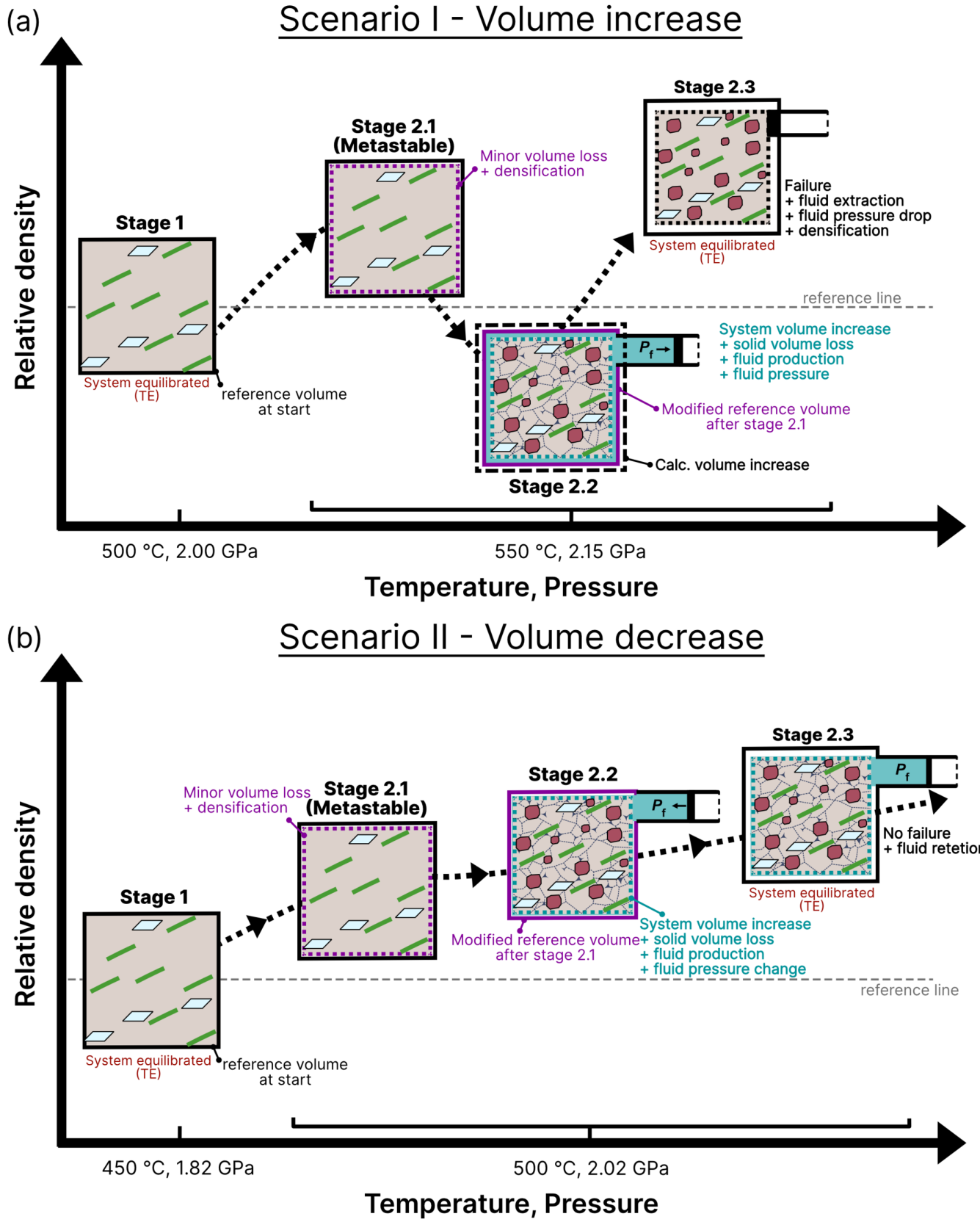


**FIGURE 7** | Legend on next page.

**FIGURE 7** | Conceptual model illustrating density and volume changes from the metastability test results. (a) Scenario I shows the system evolving through modelling stages 1 to 2.3. Stage 1 represents the initial conditions, where the system is in thermodynamic and mechanical equilibrium at 500°C and 2.00 GPa. In Stage 2, conditions increase to 550°C and 2.15 GPa. Stage 2.1, the volume of the metastable phases change, leading to densification and a decrease in total system volume. In Stage 2.2, the system reaches thermodynamic equilibrium, producing garnet and fluid. This reaction decreases the density of the system and increases the total system volume, increasing the fluid pressure, as indicated by the black arrow in the valve mechanism. Finally, in Stage 2.3, mechanical failure occurs, causing fluid extraction, which results in further densification and a reduction of the total system volume. The grey dashed line marks the reference density from Stage 1, while the black solid box remains a constant size relative to the system volume at Stage 1. (b) Scenario II follows a similar progression but begins with different initial conditions of 450°C and 1.82 GPa. In Stage 2, conditions increase to 500°C and 2.02 GPa, leading to densification and a decrease in total system volume. In Stage 2.2, the system reaches thermodynamic equilibrium, producing garnet and fluid; however, due to a steeper Clapeyron slope, the reaction leads to a further decrease in volume and a fluid pressure below lithostatic values, as indicated by the black arrow in the valve mechanism. In Stage 2.3, the system remains intact without mechanical failure, undergoing densification while retaining fluid within a fluid-filled porosity. However, fluid extraction and additional densification may still occur if the transient volume change in Stage 2.1 is large enough (see Figure 8b), particularly under differential stress. It should be noted that the microscopic representation of the process is for illustrative purposes only, and that the models discussed in the text are macroscopic. The abbreviation "TE" indicates thermodynamic equilibrium.

**TABLE 2** | Calculated volume changes associated with persistence of metastable phases.

| **Scenario I—Volume increase** | | | | |
|---|---|---|---|---|
| **System condition** | **Temperature [°C]** | **Pressure [GPa]** | **volume [cm$^3$]** | **density [g/cm$^3$]** |
| Stage 1 | 500 | 2.00 | 240.9220 | 3.1608 |
| Stage 2.1 | 550 | 2.15 | 240.8869 | 3.1612 |
| Stage 2.2 | 550 | 2.15 | 241.6341 | 3.1514 |
| Stage 2.3 | 550 | 2.15 | 239.6871 | 3.1674 |
| **Clapeyron slope d$P$/d$T$ [bar/°C]** | **$P_f$ Stage 1 –> Stage 2.2** | **$P_f$ Stage 2.1 –> Stage 2.2** | **Ratio $P_f$'s** | **Resulting pressure increase** |
| 30.0 | 1.66 | 1.71 | 1.03 | 121.0 MPa |
| **Scenario II – Volume decrease** | | | | |
| **System condition** | **Temperature [°C]** | **Pressure [GPa]** | **volume [cm$^3$]** | **density [g/cm$^3$]** |
| Stage 1 | 450 | 1.82 | 173.0722 | 3.2296 |
| Stage 2.1 | 500 | 2.02 | 172.9238 | 3.2323 |
| Stage 2.2 | 500 | 2.02 | 172.2226 | 3.2633 |
| Stage 2.3 | 500 | 2.02 | 165.6666 | 3.3455 |
| **Clapeyron slope d$P$/d$T$ [bar/°C]** | **$P_f$ Stage 1 –> Stage 2.2** | **$P_f$ Stage 2.1 –> Stage 2.2** | **Ratio $P_f$'s** | **Resulting pressure increase** |
| 41.0 | 0.88 | 0.9 | 1.02 | 39.3 MPa |

increments and a potential threshold for a maximum fluid-filled porosity. The inclusion of differential stress as an additional deformation parameter increases the sensitivity of the failure mechanism of the mechanical model to fluid production and volume changes (Figure 6). Finally, the model is discussed in terms of its applicability to natural case studies by comparing the model results with natural observations from high-pressure rocks.

## 5.1 | Reactivity of the System During Increasing Pressure and Temperature

Gibbs free energy minimisation is performed at each $P$–$T$ increment to simulate the instantaneous re-equilibration of the reactive system. This approach does not take into account the transient small volume changes that occur during the increase in $P$ and $T$ prior to the reaction if during the increment the previous mineral assemblage remains metastable. Since the molar volume of a metastable phase is pressure and temperature dependent, transient fluid pressure changes can occur prior to the reaction (see Section 2.2). To assess the effect of these volume changes, an unaltered basaltic rock composition was modelled under two scenarios: (1) a total volume increase of the system and (2) a total volume decrease of the system.

In Scenario 1, the rock system undergoes a continuous devolatilisation reaction with volume increase during garnet growth. The system evolves from an arbitrary Stage 1 at 500°C and 2 GPa to a Stage 2 at 550°C and 2.15 GPa. A much larger

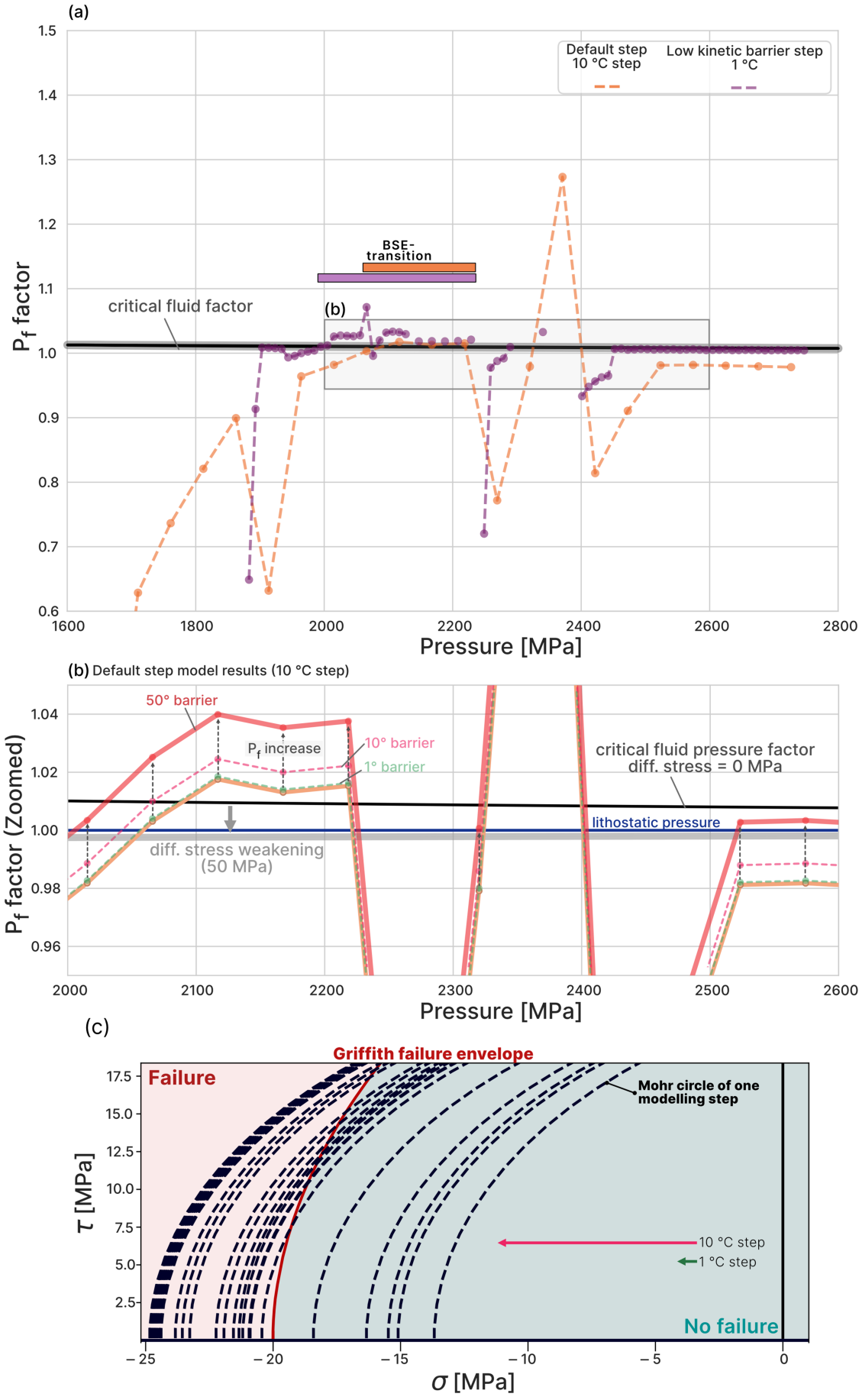


**FIGURE 8** | Legend on next page.

**FIGURE 8** | Effects of transient volume changes and the modelling increment step on the model results. a) Simulated fluid factor for two models with different kinetic barriers—one with a higher kinetic barrier (default model) and one with a lower kinetic barrier—using $S = 20$ MPa and $\Delta\delta = 50$ MPa (as in Figure 6a). Coloured bars indicate the duration of the blueschist-to-eclogite transition and the associated fluid extraction for both simulations. (b) A zoomed-in view of fluid factor values during the blueschist-to-eclogite transition and at higher pressures. The increase in fluid factor due to transient volume changes is shown for different temperature steps: 50°C (red line), 10°C (pink line) and 1°C (green line). A fluid factor of 1 corresponds to fluid pressure equal to the lithostatic pressure. The critical fluid factor exceeds 1 due to the tensile strength of the rock (black line). When differential stress increases, the critical fluid pressure can drop below 1 (grey line, using $\Delta\delta = 50$ MPa). (c) Example of Mohr–Coulomb diagram from an unmodified basalt simulation with $S$ of 20 MPa and $\Delta\delta$ of 50 MPa. Coloured regions are the fractured (red) and intact (blue) regions. Dashed black lines represent the Mohr circle at different modelling steps, with the red line indicating the failure envelope. Arrows illustrate the calculated shift of the Mohr circle when metastable feedback and temperature increments are incorporated into the failure model.

temperature increment is considered here to explore the effect of metastable persistence on the fluid pressure. At Stage 1, the predicted stable mineral assemblage consists of omphacite, muscovite, tremolite, glaucophane, epidote, hematite, lawsonite, quartz and rutile. In Stage 2, garnet and fluid become stable, along with epidote, quartz, omphacite, lawsonite and rutile. The molar volumes of the phases were calculated using Theriak. The density and volume changes at each stage are summarised in Table 2 and illustrated in Figure 7a (see Data S3 for modelling details). The Clapeyron slope for this reaction is 30 MPa/°C. At Stage 2.1, the metastable system results in only a slight densification of the system, increasing from 3.1608 g/cm$^3$ to 3.1612 g/cm$^3$, corresponding to a total system volume decrease of 0.01 vol.%. However, after re-equilibration at Stage 2.2, the system density decreases to 3.1514 g/cm$^3$, reflecting a 0.29 vol.% increase due to fluid production and the presence of a free fluid phase (Figure 7a). The transition from Stage 2.1 to Stage 2.2 is associated with an even greater increase in total system volume of 0.31 vol.%, because of the total system volume decrease of the metastable system at Stage 2.1 compared to Stage 1. In both cases, the production of fluid at Stage 2.2 results in an increase in fluid pressure as visualised by the valve mechanism in Figure 7a. The large calculation step from Stage 1 to Stage 2.2 results in a fluid factor value of 1.66 (see Equation 11), corresponding to a theoretical pre-failure fluid pressure of 3.57 GPa in a perfectly sealed system. In reality, hydraulic failure would occur before reaching this value. Similarly, the transition from Stage 2.1 to Stage 2.2 yields a fluid factor of 1.71, corresponding to 3.69 GPa. An increase of 120 MPa is observed between the two cases. Assuming no differential stress and a rock with a tensile strength of 20 MPa under a lithostatic pressure of 2.15 GPa, the critical fluid factor for pure extensional failure is given by the lithostatic pressure and the tensile strength:

$$\frac{P_{\text{lithostatic}} + S}{P_{\text{lithostatic}}} \sim 1.01. \tag{13}$$

This suggests that in both cases, the system unequivocally undergoes brittle failure at multiple stages along the $P$–$T$ path, leading to fluid extraction and an associated densification to 3.1674 g/cm$^3$ (Table 2). These results highlight the critical role of fluid pressure increases coupled with stable or metastable volume changes, which are responsible for fluid-induced brittle fracturing during metamorphism, particularly when fluid factors approach the critical threshold of 1.01. Values close to 1.01 can be identified in Figure 8a (yellow curve) during the blueschist-to-eclogite transition. The yellow curve shows the fluid factor values of the modelling results presented in Figure 6a.

In Scenario 2, the rock system undergoes a similar continuous devolatilisation reaction with volume decrease during garnet growth. The system evolves from Stage 1, at 450°C and 1.82 GPa, to Stage 2, at 500°C and 2.02 GPa. In Stage 1, the predicted mineral assemblage is clinopyroxene, chlorite, muscovite, tremolite, glaucophane, lawsonite and titanite. In Stage 2, garnet and fluid become stable, along with omphacite, muscovite, tremolite, glaucophane, lawsonite and rutile. The volume and density of the system at each stage are summarised in Table 2 and shown in Figure 7b (see Data S3 for modelling results). This modelling step represents a Clapeyron slope of 41 MPa/°C. The calculated metastable system at Stage 2.1 (Figure 7b) results in a densification of the system from 3.2296 g/cm$^{-3}$ to 3.2323 g/cm$^{-3}$ compared to Stage 1 (Table 2). This densification is associated with a total volume decrease of 0.08 vol.% (Table 2). The re-equilibration of the system at Stage 2.2 (Figure 7b) results in an increase in system density from 3.2296 g/cm$^{-3}$ to 3.2633 g/cm$^{-3}$ compared to Stage 1. This reaction to Stage 2.2 is associated with a 0.04 vol.% decrease even with the production of a free fluid phase (Table 2, Figure 7b). The calculated fluid factor between Stage 1 and Stage 2.2 of 0.88 corresponds to a fluid pressure of 1.77 GPa and to a fluid factor of 0.89 and a fluid pressure of 1.81 GPa between Stage 2.1 and Stage 2.2. This results in a fluid pressure increase of 39.2 MPa when the volume change of the metastable phases is taken into account. In both cases, the conditions are not sufficient to induce brittle failure and therefore no fluid extraction occurs.

The increase in fluid pressure becomes particularly significant as the fluid factor approaches the critical threshold. Figure 8b shows a comparison between the fluid factor of the standard model (orange curve) and the larger fluid factor in Scenario 2 (red curve). Values initially below the critical threshold rise above the threshold as a result of the transient volume changes and associated pressure changes. However, the 50°C increment used in Scenario 2 is relatively large compared to the 10°C increment used in the standard models. A smaller step size results in a less pronounced increase in the fluid factor (pink curve in Figure 8b), meaning that the transient volume change has a less critical—though still meaningful—effect. Testing even smaller $P$–$T$ increments (1°C and 100 MPa) in the metabasalt model produces a similar total volumetric fluid output compared to the result in Figure 6a (see Figure S2-7), but shows an earlier increase in the fluid factor because the major dehydration reactions of amphiboles, lawsonite and chlorite occur earlier at $P$–$T$

increments that were not encountered by the default model (see purple curve in Figure 8a). In addition, smaller *P–T* increments result in much smaller transient volume changes, as shown by the green curve in Figure 8b.

The combined effects of increment size and transient volume change are visualised in the Mohr–Coulomb diagram (Figure 8c). A 10°C increment causes a ~7 MPa fluid pressure shift (red arrow), moving the Mohr circle (dashed black) closer to the failure envelope (red). In contrast, a 1°C increment shifts it by less than 1 MPa, making failure initiation negligible. The smaller increment model simulates gradual fluid production and transient extraction during the blueschist-to-eclogite transition (Figure 8a). Veins in eclogites might suggest pulsed internal fluid release via mineral breakdown, linked to shear or tensile failure (Angiboust et al. 2011; Angiboust and Raimondo 2022; Philippot and Selverstone 1991; Strating and Vissers 1991; Taetz et al. 2018; Yamato et al. 2019; Huber et al. 2024; Giuntoli et al. 2018). This indicates fluid extraction may not always be continuous, unlike the smaller increment model. Instead, the default model, with a larger reaction barrier, better captures periodic fluid extraction during brittle failure (Figure 6a).

Additionally, Figure 8b shows that differential stress lowers the critical fluid factor below 1, similar to the transient volume change effect at a 10°C increment (pinkish line). Seismic studies observe a comparable influence: Warren-Smith et al. (2019) and Condit and French (2022) link slow slip events (SSEs) to episodic failure and fluid overpressure under 55–80 MPa differential stress, aligning with the metabasalt model. Given these observations, a minimum of 50 MPa differential stress is recommended for the integrated model, especially with a 10°C increment.

Two scenarios are considered: Scenario I represents a total system volume increase, while Scenario II represents a total system volume decrease, each corresponding to a different Clapeyron slope (see Figure 3). See text for details.

### 5.2 | Parameters of the Mechanical Model

The interplay between mechanical competence, dehydration reactions and mineral assemblage strongly influences fluid extraction. At differential stress values of several tens of MPa, the mechanical model reveals distinct lithological responses (Figure 6c,d). In weaker lithologies like serpentinite, failure at low differential stress extracts a significant portion of fluid, with shifts from extensional to shear failure occurring above 12 MPa (Figure 6d). Despite changes in failure mode, cumulative fluid extraction remains largely constant, as failure remains linked to large fluid release episodes. In contrast, the metabasalt model shows increasing stress (> 30 MPa) leads to more extraction steps and higher fluid volumes. Beyond 80 MPa, shifts in failure mode further amplify extraction events, raising cumulative fluid output by 1–2 vol.%. These results, supported by tensile strength and basaltic composition tests (Figures S2-3 and S2-4), emphasise how stress conditions and mineralogy regulate fluid release. A constant value for differential stress is a first-order assumption and a more accurate model of these mechanisms would require 2D or 3D microscopic models. Ultimately, variations in extraction frequency and volume may affect fluid distribution within the subducting slab, influencing the stability of hydrous minerals and fluid transfer to the mantle, with wider implications for mantle wedge hydration.

The model presented here predicts brittle failure as a function of volume and pressure changes, assuming all extracted fluid is released upon failure due to pore interconnectivity. In the absence of failure, fluid remains trapped as fluid-filled porosity, potentially enabling deeper transport of fluid into the mantle (Figures 5b and 6). Geophysical studies suggest high fluid pressures near lithostatic values and fluid-filled porosities up to 4 vol.% within a 5 km-thick layer of the subducting plate at 20–40 km depth, linked to oceanic crust dehydration (Abers et al. 2009; Audet et al. 2009; Egbert et al. 2022; Gosselin et al. 2020; Kodaira et al. 2004; Peacock 2009; Peacock et al. 2011; Shiina et al. 2013). For differential stresses above 30 MPa, our model predicts fluid porosities comparable to these estimates. However, at lower stresses, predicted porosities reach 6 vol.% in basaltic rock and even higher in ultramafic rock, potentially enabling fluid extraction without brittle failure. This process may correspond to grain boundary wetting (Wark et al. 2003; Yoshino et al. 2006), which suggests that fluid fractions as low as 4%—depending on the dihedral angle—can form an interconnected grain boundary network. Such a network could sustain fluid flow without requiring brittle failure and sustain permeability values as high as $10^{-12}$ m$^2$ (Wark et al. 2003; Yoshino et al. 2006).

An additional input variable in ThorPT allows users to set a fluid extraction threshold. In Figure 9, a 4 vol.% threshold is applied to the setup from Figure 6 (basalt and serpentinite compositions, tensile strengths of 20 MPa and 3 MPa and 50 MPa differential stress). Results align with previous findings, with amphibole, lawsonite, chlorite, brucite and antigorite dehydration triggering brittle failure and fluid extraction. However, in the basalt model, an extra extraction step occurs below 500°C, preceding a ~6 vol.% fluid release just above 500°C. In the serpentinite model, fluid production from brucite and antigorite breakdown (~500°C) is now coupled to the porosity threshold, extracting 10 vol.% and 6 vol.% before brittle failure, consistent with Figure 6b. Both models show that mechanical failure and porosity thresholds allow some fluid retention, enabling the transport of fluids to greater depths, supporting these aforementioned geophysical observations.

### 5.3 | Time-Integrated Fluid Flux and Permeability

Distribution of the fluid at depth is ultimately governed by the permeability of a rock, which can be estimated by the amount of fluid extracted over time calculated from the time-integrated fluid flux (Ague 2014; Bovay et al. 2021; Manning and Ingebritsen 1999). The mass of fluid produced per unit of initial volume of rock ($f_{\mathrm{mv,fluid}}$) can be calculated using

$$f_{\mathrm{mv,fluid}} = f_{\mathrm{m,fluid}} * \rho_{\mathrm{solid}} * \left(1 - f_{\mathrm{v,fluid}}\right) \quad (14)$$

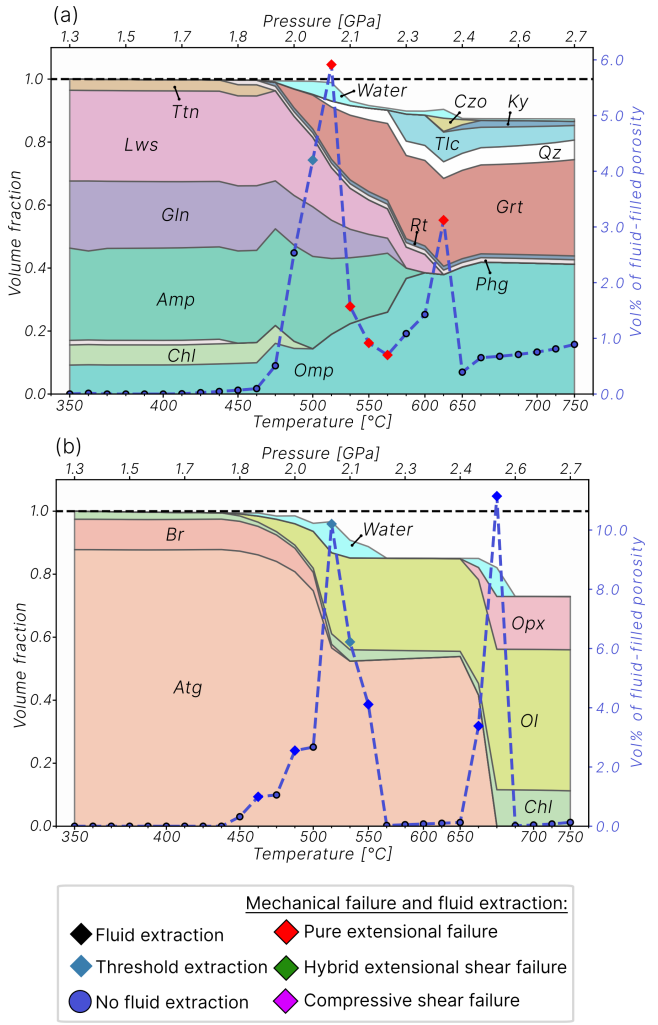


**FIGURE 9** | Mode box diagram of a metabasalt und serpentinite model including the threshold option in addition to the mechanical model. (a) Metabasalt model using a differential stress of 50 MPa and a tensile strength of 20 MPa. One additional extraction is visible marked as blue diamond, which is associated to the threshold mechanism before to brittle failure predicted also in Figure 6a. (b) Serpentinite model using a differential stress of 50 MPa and a tensile strength of 3 MPa. Two additional fluid extraction steps are visible, which are linked to the threshold mechanism before the original brittle failure compared to Figure 6b.

with $\rho_{solid}$ as the density of the solid, $f_{m,fluid}$ as the mass fraction of fluid and $f_{v,fluid}$ the volume fraction of fluid. The time-integrated fluid flux can then be calculated from

$$q_{int} = \frac{f_{mv,fluid} * L}{\rho_{fluid} * A} \quad (15)$$

with $L$ the length of the initial volume and $A$ the surface of the initial volume. By default $L$ is equal to 1 m and $A$ equal to 1 m$^2$. From this the permeability can be calculated as

$$k = \frac{q_{int}}{dt * \mu_{fluid} * g * (\rho_{solid} - \rho_{fluid})} \quad (16)$$

with $dt$ the time step, $g$ the gravitational constant, $\rho_{fluid}$ the fluid density and $\mu_{fluid}$ the fluid viscosity, which is assumed to be constant at ~$1 \times 10^{-4}$ Pas. Figure 10 shows the calculated permeability of the fluid extraction steps from the modelling results shown in Figure 9. The average time step in our simulations is approximately 0.1 Ma, corresponding to a step size of 10°C, 500 MPa and ~2 km burial depth increments. Larger or smaller step sizes will proportionally affect the magnitude of volume changes and fluid production per step, while the cumulative amount of extracted fluid stays the same, as demonstrated in the sensitivity tests provided in Figure S2-6. While these assumptions simplify the model, they may produce arbitrary absolute permeability values and timing of fluid release. Nevertheless, the calculated values of fluid extraction from the metabasalt and the serpentinite model shows a strong overlap with the values calculated for natural subducted mafic samples from the Theodul Glacier Unit (TGU) by Bovay et al. (2021).

## 5.4 | Fluid Extraction in Serpentinites and Associated Textures

Serpentinites play an important role in subduction zones due to their high fluid storage capacity and large amounts of fluid extracted during dehydration reactions (Kempf et al. 2020; Padrón-Navarta, Tommasi, et al. 2010; Schmidt and Poli 2014; Ulrich et al. 2024).

The serpentinite model presented in Figure 9b predicts a large increment of fluid production at the onset of the brucite and antigorite breakdown reaction. Multiple brittle shear failure events are predicted by the model during the first dehydration reaction of brucite and antigorite as both the amount of fluid released and the amount of olivine increase. The associated formation of olivine during brittle shear failure is consistent with the natural occurrence of textures (i) to (iv) observed in the Western Alps (Ulrich et al. 2024). Figure 10 shows the calculated permeability for the modelled fluid extraction episodes for the serpentinite (same settings as in Figure 9b). For the first episode of olivine formation and dehydration starting at ~450°C, the extracted fluid is assumed to pass over a 1 m$^2$ surface when produced from 1 m$^3$ of serpentinite. The calculation results in permeability values of $10^{-20}$ to $10^{-19}$ m$^2$ (Figure 10). Because permeability scales directly with the assumed discharge volume and surface, varying the surface area strongly affects the results: for example, assuming a smaller surface area of 0.01 m$^2$, which could represent a crack network, increases permeability by an order of magnitude with a lower limit of $10^{-18}$ m$^2$. This is relatively low compared to experiments linking a high porosity above 4 vol.% with the interconnection via dihedral angle and a permeability of $10^{-12}$ m$^2$. The model results instead represent how an interconnected fluid network with minor fluid flow could be maintained at fluid-filled porosities below 4 vol.% due to brittle failure.

A second episode of olivine formation during the final antigorite breakdown at ~670°C is associated with a large fluid production of ~10 vol.% in total (Figure 5b). The serpentinite model predicts brittle shear failure associated with the fluid production. This series of brittle failure events is associated with a second phase of olivine formation. Additionally, orthopyroxene and chlorite are predicted to be stable. These

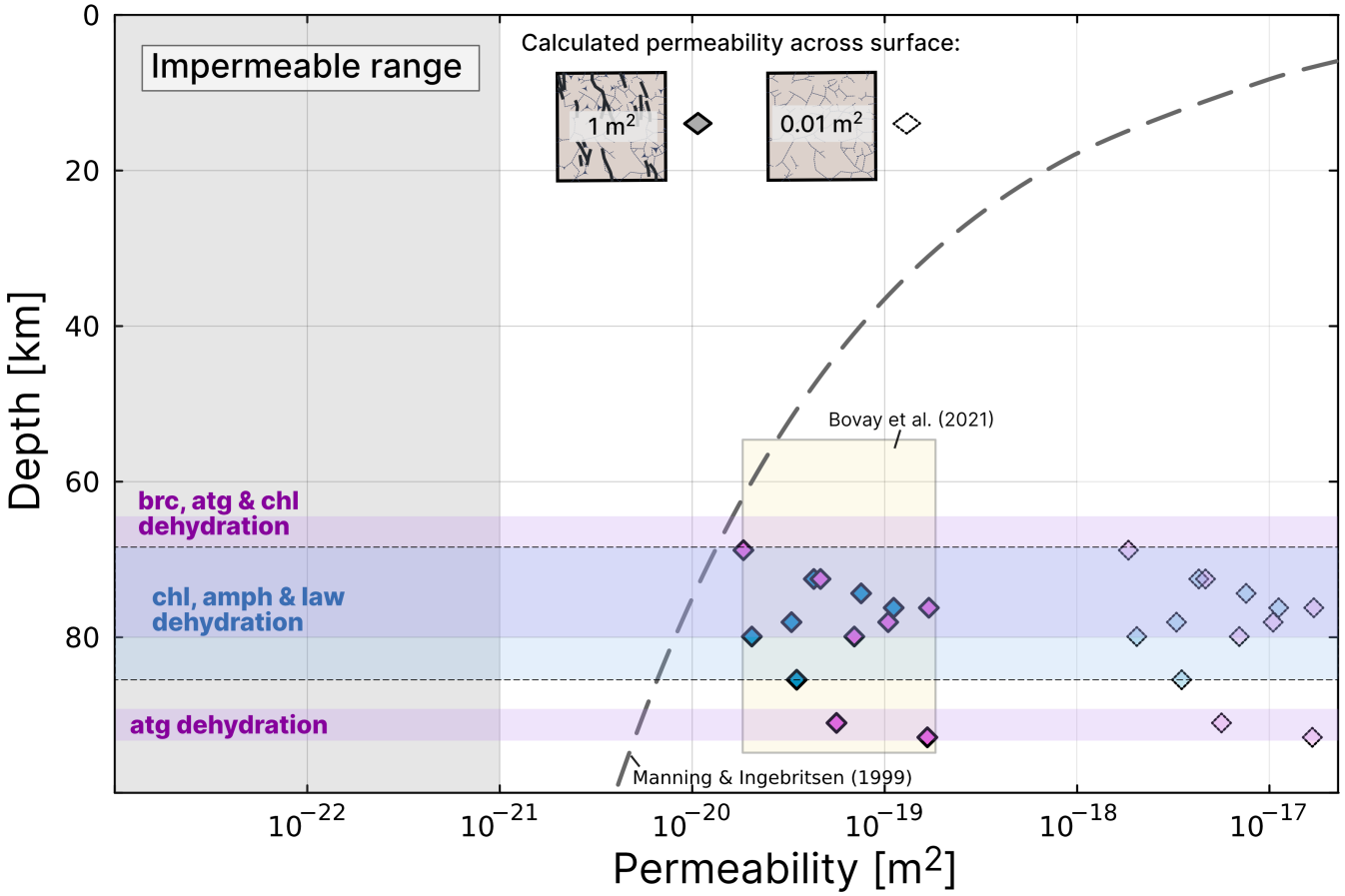


**FIGURE 10** | Calculated permeability of the metabasalt (blue diamonds) and serpentinites (purple diamonds) simulation (Figure 9) from 1 $m^3$ of rock over a discharge surface of 1 $m^2$ (filled symbols) or 0.01 $m^2$ (pale symbols). Values represent the corresponding permeability when brittle failure occurs and associated fluid is assumed to be extracted. Purple areas highlight the duration of brucite, antigorite and/or chlorite dehydration and blue area represents the dehydration of chlorite, amphiboles and lawsonite. The predicted permeability over depth estimated by Manning and Ingebritsen (1999) is shown as a grey dashed line for reference. Permeability values from natural samples from the Theodul Glacier Unit (TGU) for fluid migration the oceanic crust based on oxygen isotope data are shown in the orange field are from Bovay et al. (2021). Field of impermeability after Ganzhorn et al. (2019).

results are consistent with the textures (v) to (vii) described by Padrón-Navarta, Tommasi, et al. (2010) and Trommsdorff et al. (1998). Calculated permeability results in high values, slightly above $10^{-18}$ $m^2$, assuming the discharge surface of 0.01 $m^2$ (Figure 10). Small fractures on the micrometre to millimetre scale and grain size reduction of olivine associated with brittle failure have been documented in samples from Cerro del Almirez (Jabaloy-Sánchez et al. 2022; Padrón-Navarta, Tommasi, et al. 2010; Trommsdorff et al. 1998) and could be associated with the partial consumption of chlorite occurring after antigorite breakdown. The simulation of a dehydrating serpentinite can potentially explain brittle failure and associated textures such as for the formation of olivine in veins, shear bands and/or shear zones. The associated fluid production can therefore represent either large fluid extraction in structural conduits on the cm scale or possibly pervasive fluid flow (e.g., Bovay et al. 2021), whereas small amounts of fluid production may be accommodated on smaller pathways such as fractures or veinlets on the mm or even μm scale.

### 5.5 | Link Between Metamorphism and Seismic Activity in Subduction Zones

The build-up of fluid pressure near lithostatic values is widely proposed as a key trigger for periodic SSEs in subduction zones (Kato et al. 2010; Hyndman et al. 1997; Gao and Wang 2017; Muñoz-Montecinos et al. 2020; Behr and Bürgmann 2021; Tarling et al. 2019; Veveakis et al. 2017; Condit and French 2022; Hosokawa and Hashimoto 2022). This fluid pressure mechanism aligns with the mechanical model presented here, which shows that the transport of minor volumes of fluid-filled porosity and the build-up of fluid pressure can trigger episodic brittle failure and fluid release within the subducting lithosphere. The potential link between dehydration reactions and seismic activity remains a topic of ongoing debate in the geological community. Seismic records in active subduction zones, such as Cascadia, Shikoku, Tonga and Guerrero, are often compared to geothermal models, as metamorphic dehydration reactions are strongly influenced by the *P–T* path (e.g., Smye and England

2023; Condit et al. 2020; Hacker, Abers, and Peacock 2003; Peacock 1993).

ThorPT was used to model fluid extraction and brittle failure in unaltered MORB compositions under warm subduction zone conditions (Figure 11a). A fan-type approach with linear *P–T* paths (grey lines), similar to Rcrust (Mayne et al. 2016), was applied to account for varying Clapeyron slopes and temperature differences between the slab's top and base (Peacock 1993). The simulations used default *P–T* increments and a differential stress of 50 MPa to accommodate metastable volume changes (Figure 8). Fluid extraction was triggered when brittle failure was predicted and/or porosity exceeded 4 vol.% (Section 5.2). Figure 11b,c show that brittle failure and fluid extraction occur primarily between 400°C–550°C and 0.75–1.75 GPa, driven by chlorite dehydration and volume changes. This aligns with seismicity in warm subduction zones, particularly in Shikoku and Guerrero. A major fluid release occurs between 500°C–550°C and 1.5–2 GPa due to lawsonite, amphibole and chlorite breakdown, forming garnet, rutile, zoisite and quartz. The hydrous minerals chlorite, amphibole and lawsonite act as primary $H_2O$ carriers in basaltic compositions in subduction zones (Hernández-Uribe and Palin 2019; Peacock 1993). Brittle failure is closely tied to omphacite formation and lawsonite stability, with a major fluid release at ~520°C as chlorite breaks down completely. Experimental data suggest that omphacite growth and grain size reduction in the lawsonite-eclogite field can induce dehydration embrittlement (Incel et al. 2017), supporting the model results. At higher temperatures and pressures, brittle failure is less frequent, consistent with reduced seismicity in the upper subducting slab (Hasegawa and Nakajima 2017). These reactions support a link between dehydration, brittle failure and episodic tremor and slip events. Beyond 70 km depth, where ductile conditions dominate, minimal brittle failure is predicted (Zhan 2020). Additionally, our model results indicate that brittle-failure events are scarce along colder *P–T* paths, which represent the interior of the slab, compared to the warmer slab top. This scarcity may be linked to the observed double seismic

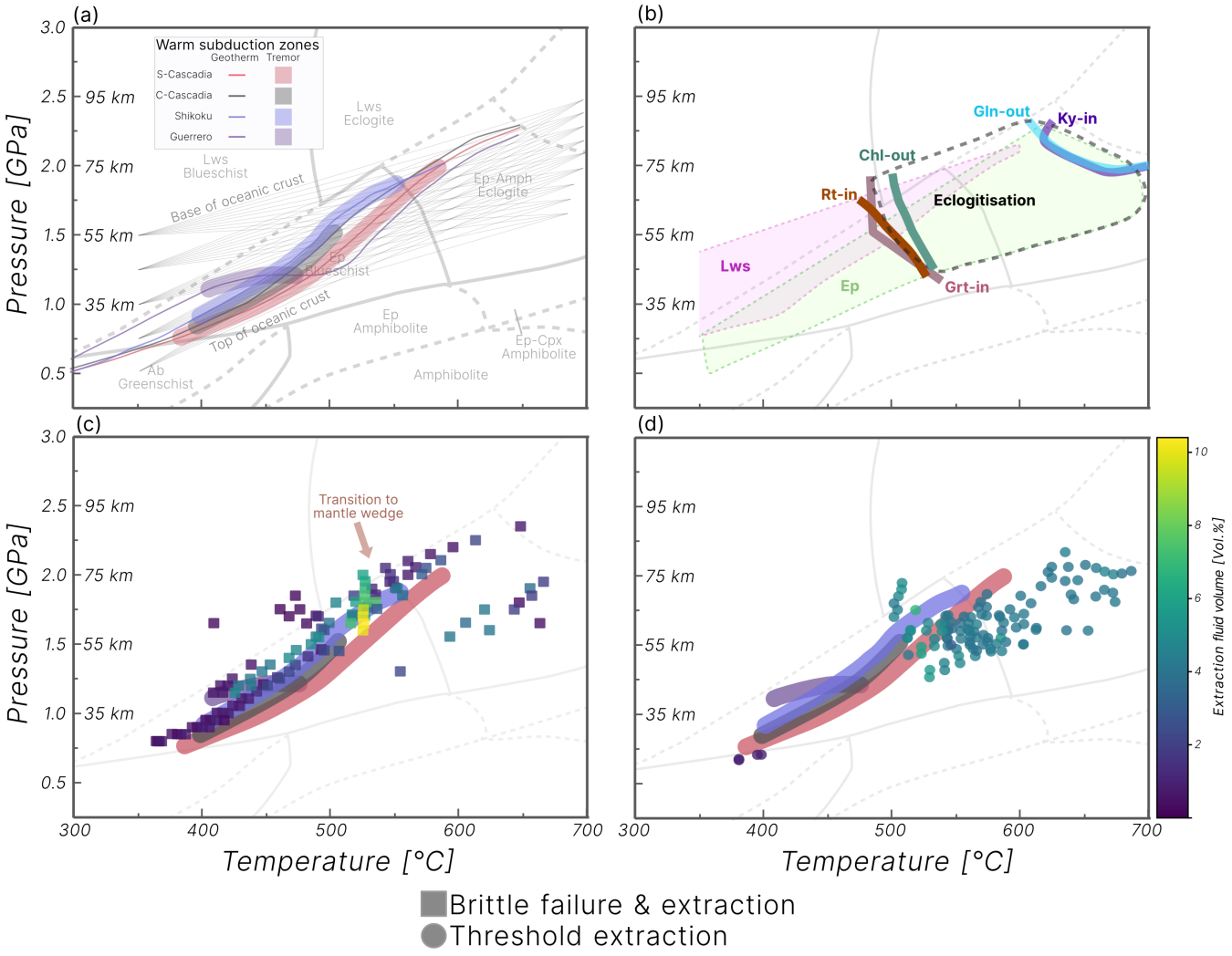


**FIGURE 11** | Brittle failure and fluid extraction in *P–T* space for a basaltic rock composition, compared with recorded seismic activity in warm subduction zones. (a) Fan-type *P–T* paths used in the model, along with *P–T* paths of warm subduction zones and corresponding seismic activity intervals from Condit et al. (2020). (b) Mineral stability fields and key mineral reactions in the evolving basaltic rock composition. (c) Predicted fluid extraction associated with brittle failure, represented as node distributions. (d) Fluid extraction driven by the threshold mechanism. Metamorphic facies are based on Forshaw et al. (2024).

zone (e.g., Hasegawa and Nakajima 2017; Igarashi et al. 2001; Hacker, Peacock, et al. 2003; Kita et al. 2006; Sippl et al. 2022). Modelling these *P–T* paths with terrigenous pelite and serpentinite (ultramafic) rock compositions reveals distinct failure patterns: the pelite model exhibits singular hybrid extensional-shear failure events, whereas the serpentinite model shows a strong association between compressive shear failure and the breakdown of hydrous phases such as chlorite, brucite and antigorite (Figure S2-7). This brittle failure in the serpentinite model, linked to hydrous phase breakdown, could further support the connection between dehydration processes and the occurrence of the double seismic zone, as suggested by Hacker, Peacock, et al. (2003).

At temperatures above 500°C, where brittle failure is not predicted, fluid is released during the blueschist-to-eclogite transition once the 4 vol.% threshold is reached, depending on amphibole stability. The accumulation of sufficient fluid volume for extraction or the build-up of fluid pressure capable of inducing brittle failure highlights the episodic nature of fluid release in subduction zones. This process may play a key role in mass transfer from the subducting slab to the mantle wedge (e.g., Hacker 2008; van Keken et al. 2011).

## 6 | Conclusion

The development of a combined petrochemical and mechanical model is critical for our understanding of how metamorphic reactions are coupled with brittle failure of rocks during major dehydration reactions. ThorPT allows the user to set up a simulation tailored to the geological problem of interest on a customised *P–T* path.

The results presented show that the volume changes caused by metamorphic reaction and associated fluid production are sufficient to initiate brittle failure even for rheologically competent materials such as basaltic rocks (represented by 20 MPa for tensile strength). Serpentinites with less competent rheologies have a higher potential for brittle failure and are more sensitive to mechanical stress. A higher mechanical resistance or low differential stress values can lead to episodic failure events.

Brittle failure and crack formation are known to increase rock permeability, and this study assumes that fluid is extracted when brittle failure occurs, in particular by hydrofracturing. In episodically failing rocks, this leads to distinct episodes of significant fluid extraction, in contrast to models that assume a continuous, gradual release of fluid within the crust. These episodic fluid extraction events further reinforce the connection between metamorphic fluids and episodic tremor and slip events in subduction zones, as suggested by numerous studies. Specifically, in basaltic crust within subduction zones, warmer geotherms—such as those near the top of the slab—promote mechanical triggering associated with dehydration reactions. This is due to volume changes occurring at lower Clapeyron slopes, enhancing the likelihood of brittle failure and fluid release.

Application of the model to subduction zone metamorphism shows that episodic and large fluid flows can be associated with brittle failure, compatible with field observations. Consequently, pulsed and localised fluid distribution in the crust may have implications for fluid migration dynamics and mass transfer.


### Acknowledgements

This project has received funding from the European Research Council (ERC) under the European Union's Horizon 2020 research. We thank Renée Tamblyn, Jacob Forshaw, Hugo Dominguez and Philip Hartmeier for fruitful discussions on petrological modelling, thermodynamic databases and two-phase flow models. This work has been greatly inspired by three anonymous reviews that have helped to improve the robustness of the mechanical model and the clarity of the paper. We also would like to thank Katy Evans for her editorial work and suggestions. Open access publishing facilitated by Universitat Bern, as part of the Wiley - Universitat Bern agreement via the Consortium Of Swiss Academic Libraries.


### Conflicts of Interest

The authors declare no conflicts of interest.

### Data Availability Statement

The data presented in this study are available in the Supporting Information (Link) and on Zenodo (10.5281/zenodo.15187881).

### Code Availability

The computer code developed in this study is open source and available via GitHub.

Name: ThorPT

Developer: Thorsten Markmann (thorsten.markmann@unibe.ch)

Available since February 26, 2023

Program language: Python (v.3.9)

Program size: 5.55 MB

Source code: https://github.com/neoscalc/ThorPT

### References


Abers, G. A., L. S. MacKenzie, S. Rondenay, Z. Zhang, A. G. Wech, and K. C. Creager. 2009. "Imaging the Source Region of Cascadia Tremor and Intermediate-Depth Earthquakes." *Geology* 37: 1119–1122. https://doi.org/10.1130/G30143A.1.

Ague, J. J. 2011. "Extreme Channelization of Fluid and the Problem of Element Mobility During Barrovian Metamorphism." *American Mineralogist* 96: 333–352. https://doi.org/10.2138/am.2011.3582.

Ague, J. J. 2014. "Fluid Flow in the Deep Crust." In *Treatise on Geochemistry: Second Edition*, 2nd ed. Elsevier Ltd. https://doi.org/10.1016/B978-0-08-095975-7.00306-5.

Angiboust, S., P. Agard, H. Raimbourg, P. Yamato, and B. Huet. 2011. "Subduction Interface Processes Recorded by Eclogite-Facies Shear Zones (Monviso, W. Alps)." *Lithos* 127: 222–238. https://doi.org/10.1016/j.lithos.2011.09.004.

Angiboust, S., and T. Raimondo. 2022. "Permeability of Subducted Oceanic Crust Revealed by Eclogite-Facies Vugs." *Geology* 50: 964–968. https://doi.org/10.1130/G50066.1.

Audet, P., M. G. Bostock, N. I. Christensen, and S. M. Peacock. 2009. "Seismic Evidence for Overpressured Subducted Oceanic Crust and Megathrust Fault Sealing." *Nature* 457: 76–78. https://doi.org/10.1038/nature07650.

Baxter, E. F., and M. J. Caddick. 2013. "Garnet Growth as a Proxy for Progressive Subduction Zone Dehydration." *Geology* 41: 643–646. https://doi.org/10.1130/G34004.1.

Bebout, G. E., and S. C. Penniston-Dorland. 2016. "Fluid and Mass Transfer at Subduction Interfaces-The Field Metamorphic Record." *Lithos* 240–243: 228–258. https://doi.org/10.1016/j.lithos.2015.10.007.

Behr, W. M., and R. Bürgmann. 2021. "What's Down There? The Structures, Materials and Environment of Deep-Seated Slow Slip and Tremor." *Philosophical Transactions. Series A, Mathematical, Physical, and Engineering Sciences* 379, no. 2193: 20200218. https://doi.org/10.1098/rsta.2020.0218.

Beinlich, A., T. John, J. C. Vrijmoed, M. Tominaga, T. Magna, and Y. Y. Podladchikov. 2020. "Instantaneous Rock Transformations in the Deep Crust Driven by Reactive Fluid Flow." *Nature Geoscience* 13: 307–311. https://doi.org/10.1038/s41561-020-0554-9.

Belgrano, T. M., and L. W. Diamond. 2019. "Subduction-Zone Contributions to Axial Volcanism in the Oman–U.A.E. Ophiolite." *Lithosphere* 11: 399–411. https://doi.org/10.1130/L1045.1.

Berman, R. G. 1988. "Internally-Consistent Thermodynamic Data for Minerals in the System Na2O-K2O-CaO-MgO-FeO-Fe2O3-Al2O3-SiO2-TiO2-H2O-CO2." *Journal of Petrology* 29, no. 2: 445–522. https://doi.org/10.1093/petrology/29.2.445.

Bovay, T., D. Rubatto, and P. Lanari. 2021. "Pervasive Fluid–Rock Interaction in Subducted Oceanic Crust Revealed by Oxygen Isotope Zoning in Garnet." *Contributions to Mineralogy and Petrology* 176: 1–22. https://doi.org/10.1007/s00410-021-01806-4.

Bras, E., P. Yamato, S. M. Schmalholz, T. Duretz, and Y. Y. Podladchikov. 2023. "Eclogitisation of Dry and Impermeable Granulite by Fluid Flow With Reaction-Induced Porosity: Insights From Hydro-Chemical Modelling." *Earth and Planetary Science Letters* 617: 118256. https://doi.org/10.1016/j.epsl.2023.118256.

Brown, T. H., and B. J. Skinner. 1974. "Theoretical Prediction of Equilibrium Phase Assemblages in Multicomponent Systems." *American Journal of Science* 274, no. 9: 961–986. https://doi.org/10.2475/ajs.274.9.961.

Bukała, M., C. J. Barnes, P. Jeanneret, et al. 2020. "Brittle Deformation During Eclogitization of Early Paleozoic Blueschist." *Frontiers in Earth Science* 8: 1–17. https://doi.org/10.3389/feart.2020.594453.

Byerlee, J. 1978. "Friction of Rocks." *PAGEOPH* 116: 615–626. https://doi.org/10.1007/BF00876528.

Carlson, W. D., D. R. M. Pattison, and M. J. Caddick. 2015. "Beyond the Equilibrium Paradigm: How Consideration of Kinetics Enhances Metamorphic Interpretation." *American Mineralogist* 100, no. 8–9: 1659–1667. https://doi.org/10.2138/am-2015-5097.

Castro, A. E., and F. S. Spear. 2016. "Reaction Overstepping and Re-Evaluation of Peak P–T Conditions of the Blueschist Unit Sifnos, Greece: Implications for the Cyclades Subduction Zone." *International Geology Review* 59, no. 5–6: 548–562. https://doi.org/10.1080/00206814.2016.1200499.

Condit, C. B., and M. E. French. 2022. "Geologic Evidence of Lithostatic Pore Fluid Pressures at the Base of the Subduction Seismogenic Zone." *Geophysical Research Letters* 49, no. 12: e2022GL098862. https://doi.org/10.1029/2022GL098862.

Condit, C. B., V. E. Guevara, J. R. Delph, and M. E. French. 2020. "Slab Dehydration in Warm Subduction Zones at Depths of Episodic Slip and Tremor." *Earth and Planetary Science Letters* 552: 116601. https://doi.org/10.1016/j.epsl.2020.116601.

Connolly, J. A. D. 1997. "Devolatilization-Generated Fluid Pressure and Deformation-Propagated Fluid Flow During Prograde Regional Metamorphism." *Journal of Geophysical Research: Solid Earth* 102, no. B8: 18149–18173. https://doi.org/10.1029/97jb00731.

Connolly, J. A. D., and Y. Y. Podladchikov. 2004. "Fluid Flow in Compressive Tectonic Settings: Implications for Midcrustal Seismic Reflectors and Downward Fluid Migration." *Journal of Geophysical Research - Solid Earth* 109: 1–12. https://doi.org/10.1029/2003JB002822.

Cox, S. F. 2010. "The Application of Failure Mode Diagrams for Exploring the Roles of Fluid Pressure and Stress States in Controlling Styles of Fracture-Controlled Permeability Enhancement in Faults and Shear Zones." *Geofluids* 10: 217–233. https://doi.org/10.1111/j.1468-8123.2010.00281.x.

Cox, S. F., M. A. Etheridge, and V. J. Wall. 1987. "The Role of Fluids in Syntectonic Mass Transport, and the Localization of Metamorphic Vein-Type Ore Deposits." *Ore Geology Reviews* 2: 65–86. https://doi.org/10.1016/0169-1368(87)90024-2.

de Capitani, C., and T. H. Brown. 1987. "The Computation of Chemical Equilibrium in Complex Systems Containing Non-Ideal Solutions." *Geochimica et Cosmochimica Acta* 51: 2639–2652. https://doi.org/10.1016/0016-7037(87)90145-1.

De Capitani, C., and K. Petrakakis. 2010. "The Computation of Equilibrium Assemblage Diagrams With Theriak/Domino Software." *American Mineralogist* 95: 1006–1016. https://doi.org/10.2138/am.2010.3354.

Diener, J. F. A., R. Powell, R. W. White, and T. J. B. Holland. 2007. "A New Thermodynamic Model for Clino- and Orthoamphiboles in the System Na 2 O–CaO–FeO–MgO–Al 2 O 3 –SiO 2 –H 2 O–O." *Journal of Metamorphic Geology* 25: 631–656. https://doi.org/10.1111/j.1525-1314.2007.00720.x.

Dominguez, H., N. Mäder, and P. Lanari. 2026. "Simulating Major Element Diffusion in Garnet Using Realistic 3D Geometries." *Computers & Geosciences* 206: 106023. https://doi.org/10.1016/j.cageo.2025.106023.

Egbert, G. D., B. Yang, P. A. Bedrosian, et al. 2022. "Fluid Transport and Storage in the Cascadia Forearc Influenced by Overriding Plate Lithology." *Nature Geoscience* 15: 677–682. https://doi.org/10.1038/s41561-022-00981-8.

Etheridge, M. A. 1983. "Differential Stress Magnitudes During Regional Deformation and Metamorphism: Upper Bound Imposed by Tensile Fracturing." *Geology* 11: 231. https://doi.org/10.1130/0091-7613(1983)11<231:DSMDRD>2.0.CO;2.

Etheridge, M. A., N. R. Daczko, T. Chapman, and C. A. Stuart. 2021. "Mechanisms of Melt Extraction During Lower Crustal Partial Melting." *Journal of Metamorphic Geology* 39: 57–75. https://doi.org/10.1111/jmg.12561.

Etheridge, M. A., V. J. Wall, and R. H. Vernon. 1983. "The Role of the Fluid Phase During Regional Metamorphism and Deformation." *Journal of Metamorphic Geology* 1: 205–226. https://doi.org/10.1111/j.1525-1314.1983.tb00272.x.

Evans, O., M. Spiegelman, and P. B. Kelemen. 2020. "Phase-Field Modeling of Reaction-Driven Cracking: Determining Conditions for Extensive Olivine Serpentinization." *Journal of Geophysical Research: Solid Earth* 125, no. 1: e2019JB018614. https://doi.org/10.1029/2019jb018614.

Ferry, J. M., and M. L. Gerdes. 1998. "Chemically Reactive Fluid Flow During Metamorphism." *Annual Review of Earth and Planetary Sciences* 26: 255–287. https://doi.org/10.1146/annurev.earth.26.1.255.

Forshaw, J. B., H. Dominguez, T. A. Markmann, et al. 2024. "Major-Element Geochemistry and Fe3+/ΣFe of Metabasites." *Journal of Petrology* 65, no. 12: egae120. https://doi.org/10.1093/petrology/egae120.

Gale, A., C. A. Dalton, C. H. Langmuir, Y. Su, and J. Schilling. 2013. "The Mean Composition of Ocean Ridge Basalts." *Geochemistry, Geophysics, Geosystems* 14: 489–518. https://doi.org/10.1029/2012GC004334.

Ganzhorn, A. C., H. Pilorgé, and B. Reynard. 2019. "Porosity of Metamorphic Rocks and Fluid Migration Within Subduction

Interfaces." *Earth and Planetary Science Letters* 522: 107–117. https://doi.org/10.1016/j.epsl.2019.06.030.

Gao, X., and K. Wang. 2017. "Rheological Separation of the Megathrust Seismogenic Zone and Episodic Tremor and Slip." *Nature* 543, no. 7645: 416–419. https://doi.org/10.1038/nature21389.

Gerya, T. V., B. Stöckhert, and A. L. Perchuk. 2002. "Exhumation of High-Pressure Metamorphic Rocks in a Subduction Channel: A Numerical Simulation." *Tectonics* 21: 6-1–6–19. https://doi.org/10.1029/2002TC001406.

Gies, N. B., M. Konrad-Schmolke, and J. Hermann. 2024. "Modeling the Global Water Cycle—The Effect of Mg-Sursassite and Phase a on Deep Slab Dehydration and the Global Subduction Zone Water Budget." *Geochemistry, Geophysics, Geosystems* 25, no. 3: e2024GC011507. https://doi.org/10.1029/2024GC011507.

Giuntoli, F., L. Menegon, G. Siron, et al. 2024. "Methane-Hydrogen-Rich Fluid Migration May Trigger Seismic Failure in Subduction Zones at Forearc Depths." *Nature Communications* 15: 480. https://doi.org/10.1038/s41467-023-44641-w.

Giuntoli, F., P. Lanari, and M. Engi. 2018. "Deeply Subducted Continental Fragments – Part 1: Fracturing, Dissolution–Precipitation, and Diffusion Processes Recorded by Garnet Textures of the Central Sesia Zone (Western Italian Alps)." *Solid Earth* 9, no. 1: 167–189. https://doi.org/10.5194/se-9-167-2018.

Gold, T., and S. Soter. 1984. "Fluid Ascent Through the Solid Lithosphere and Its Relation to Earthquakes." *Pure and Applied Geophysics* 122: 492–530. https://doi.org/10.1007/BF00874614.

Gosselin, J. M., P. Audet, C. Estève, M. McLellan, S. G. Mosher, and A. J. Schaeffer. 2020. "Seismic Evidence for Megathrust Fault-Valve Behavior During Episodic Tremor and Slip." *Science Advances* 6: eaay5174. https://doi.org/10.1126/sciadv.aay5174.

Griffits, A. A. 1921. "VI. The Phenomena of Rupture and Flow in Solids." *Philosophical Transactions of the Royal Society of London. Series A, Containing Papers of a Mathematical or Physical Character* 221: 163–198. https://doi.org/10.1098/rsta.1921.0006.

Hacker, B. R. 2008. "H2O Subduction Beyond Arcs." *Geochemistry, Geophysics, Geosystems* 9: Q03001. https://doi.org/10.1029/2007GC001707.

Hacker, B. R., G. A. Abers, and S. M. Peacock. 2003. "Subduction Factory 1. Theoretical Mineralogy, Densities, Seismic Wave Speeds, and H 2 O Contents." *Journal of Geophysical Research - Solid Earth* 108: 1–26. https://doi.org/10.1029/2001JB001127.

Hacker, B. R., S. M. Peacock, G. A. Abers, and S. D. Holloway. 2003. "Subduction Factory 2. Are Intermediate-Depth Earthquakes in Subducting Slabs Linked to Metamorphic Dehydration Reactions?" *Journal of Geophysical Research: Solid Earth* 108, no. B1. https://doi.org/10.1029/2001JB001129.

Halbach, H., and N. D. Chatterjee. 1982. "An Empirical Redlich-Kwong-Type Equation of State for Water to 1,000°C and 200 Kbar." *Contributions to Mineralogy and Petrology* 79: 337–345. https://doi.org/10.1007/BF00371526.

Hasegawa, A., and J. Nakajima. 2017. "Seismic Imaging of Slab Metamorphism and Genesis of Intermediate-Depth Intraslab Earthquakes." *Progress in Earth and Planetary Science* 4: 12. https://doi.org/10.1186/s40645-017-0126-9.

Hermann, J., O. Müntener, and M. Scambelluri. 2000. "The Importance of Serpentinite Mylonites for Subduction and Exhumation of Oceanic Crust." *Tectonophysics* 327, no. 3–4: 225–238. https://doi.org/10.1016/s0040-1951(00)00171-2.

Hernández-Uribe, D., and R. M. Palin. 2019. "A Revised Petrological Model for Subducted Oceanic Crust: Insights From Phase Equilibrium Modelling." *Journal of Metamorphic Geology* 37: 745–768. https://doi.org/10.1111/jmg.12483.

Hobbs, B. E., and A. Ord. 2018. "Coupling of Fluid Flow to Permeability Development in Mid- To Upper Crustal Environments: A Tale of Three Pressures." *Geological Society, London, Special Publications* 453: 81–120. https://doi.org/10.1144/SP453.9.

Hobbs, B. E., A. Ord, M. I. Spalla, G. Gosso, and M. Zucali. 2010. "The Interaction of Deformation and Metamorphic Reactions." *Geological Society, London, Special Publications* 332, no. 1: 189–223. https://doi.org/10.1144/sp332.12.

Holland, T., and R. Powell. 1991. "A Compensated-Redlich-Kwong (CORK) Equation for Volumes and Fugacities of CO2 and H2O in the Range 1 Bar to 50 Kbar and 100°C–1600°C." *Contributions to Mineralogy and Petrology* 109: 265–273. https://doi.org/10.1007/BF00306484.

Holland, T., and R. Powell. 1996. "Thermodynamics of Order-Disorder in Minerals; II, Symmetric Formalism Applied to Solid Solutions." *American Mineralogist* 81: 1425–1437. https://doi.org/10.2138/am-1996-11-1215.

Holland, T., and R. Powell. 2003. "Activity-Composition Relations for Phases in Petrological Calculations: An Asymmetric Multicomponent Formulation." *Contributions to Mineralogy and Petrology* 145: 492–501. https://doi.org/10.1007/s00410-003-0464-z.

Holland, T. J. B., and R. Powell. 1998. "An Internally Consistent Thermodynamic Data Set for Phases of Petrological Interest." *Journal of Metamorphic Geology* 16: 309–343. https://doi.org/10.1111/j.1525-1314.1998.00140.x.

Holland, T., J. Baker, and R. Powell. 1998. "Mixing Properties and Activity? Composition Relationships of Chlorites in the System MgO-FeO-Al2O3-SiO2-H2O." *European Journal of Mineralogy* 10: 395–406. https://doi.org/10.1127/ejm/10/3/0395.

Hosokawa, T., and Y. Hashimoto. 2022. "Geological Constraints on Dynamic Changes of Fluid Pressure in Seismic Cycles." *Scientific Reports* 12: 14789. https://doi.org/10.1038/s41598-022-19083-x.

Huber, K., J. C. Vrijmoed, and T. John. 2022. "Formation of Olivine Veins by Reactive Fluid Flow in a Dehydrating Serpentinite." *Geochemistry, Geophysics, Geosystems* 23, no. 6: e2021GC010267. https://doi.org/10.1029/2021gc010267.

Huber, K., T. John, J. C. Vrijmoed, J. Pleuger, and X. Zhong. 2024. "Pulsed Fluid Release From Subducting Slabs Caused by a Scale-Invariant Dehydration Process." *Earth and Planetary Science Letters* 644: 118924. https://doi.org/10.1016/j.epsl.2024.118924.

Hyndman, R. D., M. Yamano, and D. A. Oleskevich. 1997. "The Seismogenic Zone of Subduction Thrust Faults." *Island Arc* 6, no. 3: 244–260. https://doi.org/10.1111/j.1440-1738.1997.tb00175.x.

Igarashi, T., T. Matsuzawa, N. Umino, and A. Hasegawa. 2001. "Spatial Distribution of Focal Mechanisms for Interplate and Intraplate Earthquakes Associated With the Subducting Pacific Plate Beneath the Northeastern Japan arc: A Triple-Planed Deep Seismic Zone." *Journal of Geophysical Research* 106, no. B2: 2177–2191. https://doi.org/10.1029/2000JB900386.

Incel, S., N. Hilairet, L. Labrousse, et al. 2017. "Laboratory Earthquakes Triggered During Eclogitization of Lawsonite-Bearing Blueschist." *Earth and Planetary Science Letters* 459: 320–331. https://doi.org/10.1016/j.epsl.2016.11.047.

Jabaloy-Sánchez, A., V. L. Sánchez-Vizcaíno, J. A. Padrón-Navarta, K. Hidas, M. T. Gómez-Pugnaire, and C. J. Garrido. 2022. "Olivine-Rich Veins in High-Pressure Serpentinites: A far-Field Paleo-Stress Snapshot During Subduction." *Journal of Structural Geology* 163: 104721. https://doi.org/10.1016/j.jsg.2022.104721.

Jaeger, J., N. Cook, and R. Zimmerman. 2007. *Fundamentals of Rock Mechanics*. Cambridge University Press. https://doi.org/10.1017/CBO9780511735349.

Jamtveit, B., A. Malthe-Sørenssen, and O. Kostenko. 2008. "Reaction Enhanced Permeability During Retrogressive Metamorphism." *Earth*

*and Planetary Science Letters* 267, no. 3–4: 620–627. https://doi.org/10.1016/j.epsl.2007.12.016.

Jung, H., H. W. Green II, and L. F. Dobrzhinetskaya. 2004. "Intermediate-Depth Earthquake Faulting by Dehydration Embrittlement With Negative Volume Change." *Nature* 428: 545–549. https://doi.org/10.1038/nature02412.

Kato, A., T. Iidaka, R. Ikuta, et al. 2010. "Variations of Fluid Pressure Within the Subducting Oceanic Crust and Slow Earthquakes." *Geophysical Research Letters* 37: 1–5. https://doi.org/10.1029/2010GL043723.

Kempf, E. D., J. Hermann, E. Reusser, L. P. Baumgartner, and P. Lanari. 2020. "The Role of the Antigorite + Brucite to Olivine Reaction in Subducted Serpentinites (Zermatt, Switzerland)." *Swiss Journal of Geosciences* 113, no. 1: 16. https://doi.org/10.1186/s00015-020-00368-0.

Kerrick, D. M., and J. A. D. Connolly. 2001. "Metamorphic Devolatilization of Subducted Oceanic Metabasalts: Implications for Seismicity, arc Magmatism and Volatile Recycling." *Earth and Planetary Science Letters* 189: 19–29. https://doi.org/10.1016/S0012-821X(01)00347-8.

Kirby, S. H., S. Stein, E. A. Okal, and D. C. Rubie. 1996. "Metastable Mantle Phase Transformations and Deep Earthquakes in Subducting Oceanic Lithosphere." *Reviews of Geophysics* 34: 261–306. https://doi.org/10.1029/96RG01050.

Kita, S., T. Okada, J. Nakajima, T. Matsuzawa, and A. Hasegawa. 2006. "Existence of a Seismic Belt in the Upper Plane of the Double Seismic Zone Extending in the Along-Arc Direction at Depths of 70–100 km Beneath NE Japan." *Geophysical Research Letters* 33, no. 24. https://doi.org/10.1029/2006gl028239.

Kodaira, S., T. Iidaka, A. Kato, J.-O. Park, T. Iwasaki, and Y. Kaneda. 2004. "High Pore Fluid Pressure may Cause Silent Slip in the Nankai Trough." *Science* 1979, no. 304: 1295–1298. https://doi.org/10.1126/science.1096535.

Kohn, M. J. 1993. "Modeling of Prograde Mineral δ18O Changes in Metamorphic Systems." *Contributions to Mineralogy and Petrology* 113, no. 2: 249–261. https://doi.org/10.1007/bf00283232.

Konrad-Schmolke, M., J. Babist, M. R. Handy, and P. J. O'Brien. 2006. "The Physico-Chemical Properties of a Subducted Slab from Garnet Zonation Patterns (Sesia Zone, Western Alps)." *Journal of Petrology* 47, no. 11: 2123–2148. https://doi.org/10.1093/petrology/egl039.

Konrad-Schmolke, M., R. Halama, D. Chew, C. Heuzé, J. De Hoog, and H. Ditterova. 2023. "Discrimination of Thermodynamic and Kinetic Contributions to the Heavy Rare Earth Element Patterns in Metamorphic Garnet." *Journal of Metamorphic Geology* 41, no. 4: 465–490. https://doi.org/10.1111/jmg.12703.

Konrad-Schmolke, M., M. R. Handy, J. Babist, and P. J. O'Brien. 2005. "Thermodynamic Modelling of Diffusion-Controlled Garnet Growth." *Contributions to Mineralogy and Petrology* 149, no. 2: 181–195. https://doi.org/10.1007/s00410-004-0643-6.

Konrad-Schmolke, M., P. J. O'Brien, C. de Capitani, and D. A. Carswell. 2008. "Garnet Growth at High- and Ultra-High Pressure Conditions and the Effect of Element Fractionation on Mineral Modes and Composition." *Lithos* 103, no. 3–4: 309–332. https://doi.org/10.1016/j.lithos.2007.10.007.

Konrad-Schmolke, M., T. Zack, P. J. O'Brien, and M. Barth. 2011. "Fluid Migration Above a Subducted Slab - Thermodynamic and Trace Element Modelling of Fluid–Rock Interaction in Partially Overprinted Eclogite-Facies Rocks (Sesia Zone, Western Alps)." *Earth and Planetary Science Letters* 311: 287–298. https://doi.org/10.1016/j.epsl.2011.09.025.

Konrad-Schmolke, M., T. Zack, P. J. O'Brien, and D. E. Jacob. 2008. "Combined Thermodynamic and Rare Earth Element Modelling of Garnet Growth During Subduction: Examples from Ultrahigh-Pressure Eclogite of the Western Gneiss Region, Norway." *Earth and Planetary Science Letters* 272, no. 1–2: 488–498. https://doi.org/10.1016/j.epsl.2008.05.018.

Lanari, P., and E. Duesterhoeft. 2019. "Modeling Metamorphic Rocks Using Equilibrium Thermodynamics and Internally Consistent Databases: Past Achievements, Problems and Perspectives." *Journal of Petrology* 60: 19–56. https://doi.org/10.1093/petrology/egy105.

Lanari, P., and M. Engi. 2017. "Local Bulk Composition Effects on Metamorphic Mineral Assemblages." *Reviews in Mineralogy and Geochemistry* 83: 55–102. https://doi.org/10.2138/rmg.2017.83.3.

Liu, J.-H., P. Lanari, R. Tamblyn, et al. 2025. "Ultra-Fast Metamorphic Reaction During Regional Metamorphism." *Geochimica et Cosmochimica Acta* 394: 106–125. https://doi.org/10.1016/j.gca.2025.01.036.

Malvoisin, B., Y. Y. Podladchikov, and J. C. Vrijmoed. 2015. "Coupling Changes in Densities and Porosity to Fluid Pressure Variations in Reactive Porous Fluid Flow: Local Thermodynamic Equilibrium." *Geochemistry, Geophysics, Geosystems* 16: 4362–4387. https://doi.org/10.1002/2015GC006019.

Manning, C. E., and S. E. Ingebritsen. 1999. "Permeability of the Continental Crust: Implications of Geothermal Data and Metamorphic Systems." *Reviews of Geophysics* 37: 127–150. https://doi.org/10.1029/1998RG900002.

Mayne, M. J., J. -F. Moyen, G. Stevens, and L. Kaislaniemi. 2016. "Rcrust: A Tool for Calculating Path-Dependent Open System Processes and Application to Melt Loss." *Journal of Metamorphic Geology* 34, no. 7: 663–682. https://doi.org/10.1111/jmg.12199.

Mazzucchelli, M. L., E. Moulas, B. J. P. Kaus, and T. Speck. 2024. "Fluid–Mineral Equilibrium Under Nonhydrostatic Stress: Insight From Molecular Dynamics." *American Journal of Science* 324: 1–29. https://doi.org/10.2475/001c.92881.

McKenzie, D. 1984. "The Generation and Compaction of Partially Molten Rock." *Journal of Petrology* 25: 713–765. https://doi.org/10.1093/petrology/25.3.713.

Morishige, M., and P. E. van Keken. 2018. "Fluid Migration in a Subducting Viscoelastic Slab." *Geochemistry, Geophysics, Geosystems* 19: 337–355. https://doi.org/10.1002/2017GC007236.

Moulas, E., S. M. Schmalholz, Y. Podladchikov, L. Tajčmanová, D. Kostopoulos, and L. Baumgartner. 2019. "Relation Between Mean Stress, Thermodynamic, and Lithostatic Pressure." *Journal of Metamorphic Geology* 37: 1–14. https://doi.org/10.1111/jmg.12446.

Moulas, E., B. Kaus, and B. Jamtveit. 2022. "Dynamic Pressure Variations in the Lower Crust Caused by Localized Fluid-Induced Weakening." *Communications Earth & Environment* 3, no. 1: 157. https://doi.org/10.1038/s43247-022-00478-7.

Muñoz-Montecinos, J., S. Angiboust, A. Cambeses, and A. García-Casco. 2020. "Multiple Veining in a Paleo–Accretionary Wedge: The Metamorphic Rock Record of Prograde Dehydration and Transient High Pore-Fluid Pressures Along the Subduction Interface (Western Series, Central Chile)." *Geosphere* 16, no. 3: 765–786. https://doi.org/10.1130/ges02227.1.

Muñoz-Montecinos, J., S. Angiboust, C. Minnaert, et al. 2024. "Fluid-Driven Shear Instabilities in the Subducted Oceanic Mantle at Intermediate Depths: Insights From Western Alps Meta-Ophiolites." *Geochemistry, Geophysics, Geosystems* 25, no. 8. https://doi.org/10.1029/2024gc011581.

Nerone, S., C. Groppo, and F. Rolfo. 2023. "Equilibrium and Kinetic Approaches to Understand the Occurrence of the Uncommon Chloritoid + Biotite Assemblage." *European Journal of Mineralogy* 35: 305–320. https://doi.org/10.5194/ejm-35-305-2023.

Nguyen, T. T. N., M. N. Vu, N. H. Tran, N. H. Dao, and D. T. Pham. 2020. "Stress Induced Permeability Changes in Brittle Fractured Porous

Rock." *International Journal of Rock Mechanics and Mining Sciences* 127: 104224. https://doi.org/10.1016/j.ijrmms.2020.104224.

Niu, F., P. G. Silver, R. M. Nadeau, and T. V. McEvilly. 2003. "Migration of Seismic Scatterers Associated With the 1993 Parkfield Aseismic Transient Event." *Nature* 426: 544–548. https://doi.org/10.1038/nature02151.

Nordstrom, D. K., and J. L. Munoz. 1994. *Geochemical Thermodynamics*. 2nd ed. Blackwell Scientific Publications.

Norton, D., and R. Knapp. 1977. "Transport Phenomena in Hydrothermal Systems; The Nature of Porosity." *American Journal of Science* 277, no. 8: 913–936. https://doi.org/10.2475/ajs.277.8.913.

Okamoto, A., and H. Shimizu. 2015. "Contrasting Fracture Patterns Induced by Volume-Increasing and -Decreasing Reactions: Implications for the Progress of Metamorphic Reactions." *Earth and Planetary Science Letters* 417: 9–18. https://doi.org/10.1016/j.epsl.2015.02.015.

Okamoto, A., H. Shimizu, J. Fukuda, J. Muto, and T. Okudaira. 2017. "Reaction-Induced Grain Boundary Cracking and Anisotropic Fluid Flow During Prograde Devolatilization Reactions Within Subduction Zones." *Contributions to Mineralogy and Petrology* 172, no. 9: 75. https://doi.org/10.1007/s00410-017-1393-6.

Padrón-Navarta, J. A., A. Tommasi, C. J. Garrido, et al. 2010. "Fluid Transfer Into the Wedge Controlled by High-Pressure Hydrofracturing in the Cold top-Slab Mantle." *Earth and Planetary Science Letters* 297: 271–286. https://doi.org/10.1016/j.epsl.2010.06.029.

Padrón-Navarta, J. A., J. Hermann, C. J. Garrido, V. López Sánchez-Vizcaíno, and M. T. Gómez-Pugnaire. 2010. "An Experimental Investigation of Antigorite Dehydration in Natural Silica-Enriched Serpentinite." *Contributions to Mineralogy and Petrology* 159, no. 1: 25–42. https://doi.org/10.1007/s00410-009-0414-5.

Pattison, D. R. M., and D. K. Tinkham. 2009. "Interplay Between Equilibrium and Kinetics in Prograde Metamorphism of Pelites: An Example From the Nelson Aureole, British Columbia." *Journal of Metamorphic Geology* 27, no. 4: 249–279. https://doi.org/10.1111/j.1525-1314.2009.00816.x.

Pattison, D. R. M., C. de Capitani, and F. Gaidies. 2011. "Petrological Consequences of Variations in Metamorphic Reaction Affinity." *Journal of Metamorphic Geology* 29: 953–977. https://doi.org/10.1111/j.1525-1314.2011.00950.x.

Peacock, S. M. 1993. "The Importance of Blueschist Eclogite Dehydration Reactions in Subducting Oceanic Crust." *GSA Bulletin* 105, no. 5: 684–694. https://doi.org/10.1130/0016-7606(1993)105<0684:TIOBED>2.3.CO;2.

Peacock, S. M. 2009. "Thermal and Metamorphic Environment of Subduction Zone Episodic Tremor and Slip." *Journal of Geophysical Research* 114: B00A07. https://doi.org/10.1029/2008JB005978.

Peacock, S. M., N. I. Christensen, M. G. Bostock, and P. Audet. 2011. "High Pore Pressures and Porosity at 35 km Depth in the Cascadia Subduction Zone." *Geology* 39: 471–474. https://doi.org/10.1130/G31649.1.

Penniston-Dorland, S. C., M. J. Kohn, and C. E. Manning. 2015. "The Global Range of Subduction Zone Thermal Structures From Exhumed Blueschists and Eclogites: Rocks Are Hotter Than Models." *Earth and Planetary Science Letters* 428: 243–254. https://doi.org/10.1016/j.epsl.2015.07.031.

Philippot, P., and J. Selverstone. 1991. "Trace-Element-Rich Brines in Eclogitic Veins: Implications for Fluid Composition and Transport During Subduction." *Contributions to Mineralogy and Petrology* 106: 417–430. https://doi.org/10.1007/BF00321985.

Plümper, O., A. Botan, C. Los, Y. Liu, A. Malthe-Sørenssen, and B. Jamtveit. 2017. "Fluid-Driven Metamorphism of the Continental Crust Governed by Nanoscale Fluid Flow." *Nature Geoscience* 10: 685–690. https://doi.org/10.1038/ngeo3009.

Plümper, O., A. Røyne, A. Magrasó, and B. Jamtveit. 2012. "The Interface-Scale Mechanism of Reaction-Induced Fracturing During Serpentinization." *Geology* 40: 1103–1106. https://doi.org/10.1130/G33390.1.

Plümper, O., D. Wallis, F. Teuling, et al. 2022. "High-Magnitude Stresses Induced by Mineral-Hydration Reactions." *Geology* 50, no. 12: 1351–1355. https://doi.org/10.1130/g50493.1.

Plümper, O., T. John, Y. Y. Podladchikov, J. C. Vrijmoed, and M. Scambelluri. 2017. "Fluid Escape From Subduction Zones Controlled by Channel-Forming Reactive Porosity." *Nature Geoscience* 10: 150–156. https://doi.org/10.1038/ngeo2865.

Powell, R., K. A. Evans, E. C. R. Green, and R. W. White. 2018. "On Equilibrium in Non-Hydrostatic Metamorphic Systems." *Journal of Metamorphic Geology* 36: 419–438. https://doi.org/10.1111/jmg.12298.

Putnis, A. 2015. "Transient Porosity Resulting From Fluid–Mineral Interaction and Its Consequences." *Reviews in Mineralogy and Geochemistry* 80, no. 1: 1–23. https://doi.org/10.2138/rmg.2015.80.01.

Ramsay, J. G. 1980. "The Crack–Seal Mechanism of Rock Deformation." *Nature* 284: 135–139. https://doi.org/10.1038/284135a0.

Rubie, D. C. 1986. "The Catalysis of Mineral Reactions by Water and Restrictions on the Presence of Aqueous Fluid During Metamorphism." *Mineralogical Magazine* 50, no. 357: 399–415. https://doi.org/10.1180/minmag.1986.050.357.05.

Saffer, D. M., and H. J. Tobin. 2011. "Hydrogeology and Mechanics of Subduction Zone Forearcs: Fluid Flow and Pore Pressure." *Annual Review of Earth and Planetary Sciences* 39: 157–186. https://doi.org/10.1146/annurev-earth-040610-133408.

Schmalholz, S. M., E. Moulas, L. Räss, and O. Müntener. 2023. "Serpentinite Dehydration and Olivine Vein Formation During Ductile Shearing: Insights From 2D Numerical Modeling on Porosity Generation, Density Variations, and Transient Weakening." *Journal of Geophysical Research: Solid Earth* 128, no. 11: e2023JB026985. https://doi.org/10.1029/2023jb026985.

Schmidt, M. W., and S. Poli. 2014. "Devolatilization During Subduction." In *Treatise on Geochemistry*, 669–701. Elsevier. https://doi.org/10.1016/B978-0-08-095975-7.00321-1.

Schwarz, J. O., M. Engi, and A. Berger. 2011. "Porphyroblast Crystallization Kinetics: The Role of the Nutrient Production Rate." *Journal of Metamorphic Geology* 29: 497–512. https://doi.org/10.1111/j.1525-1314.2011.00927.x.

Secor, D. T. T. 1965. "Role of Fluid Pressure in Jointing." *American Journal of Science* 263: 633–646. https://doi.org/10.2475/ajs.263.8.633.

Shiina, T., J. Nakajima, and T. Matsuzawa. 2013. "Seismic Evidence for High Pore Pressures in the Oceanic Crust: Implications for Fluid-Related Embrittlement." *Geophysical Research Letters* 40: 2006–2010. https://doi.org/10.1002/grl.50468.

Sibson, R. H. 2000. "A Brittle Failure Mode Plot Defining Conditions for High-Flux Flow." *Economic Geology* 95: 41–48. https://doi.org/10.2113/gsecongeo.95.1.41.

Sibson, R. H. 2013. "Stress Switching in Subduction Forearcs: Implications for Overpressure Containment and Strength Cycling on Megathrusts." *Tectonophysics* 600: 142–152. https://doi.org/10.1016/j.tecto.2013.02.035.

Sibson, R. H. 2017. "Tensile Overpressure Compartments on Low-Angle Thrust Faults." *Earth, Planets and Space* 69: 113. https://doi.org/10.1186/s40623-017-0699-y.

Sippl, C., B. Schurr, G. Asch, and J. Kummerow. 2018. "Seismicity Structure of the Northern Chile Forearc From >100,000 Double-Difference

Relocated Hypocenters." *Journal of Geophysical Research - Solid Earth* 123: 4063–4087. https://doi.org/10.1002/2017JB015384.

Sippl, C., A. Dielforder, T. John, and S. M. Schmalholz. 2022. "Global Constraints on Intermediate-Depth Intraslab Stresses From Slab Geometries and Mechanisms of Double Seismic Zone Earthquakes." *Geochemistry, Geophysics, Geosystems* 23, no. 9: e2022GC010498. https://doi.org/10.1029/2022gc010498.

Smye, A. J., and P. C. England. 2023. "Metamorphism and Deformation on Subduction Interfaces: 2. Petrological and Tectonic Implications." *Geochemistry, Geophysics, Geosystems* 24, no. 1: e2022GC010645. https://doi.org/10.1029/2022gc010645.

Spear, F. S., and R. M. Pattison. 2017. "The Implications of Overstepping for Metamorphic Assemblage Diagrams (MADs)." *Chemical Geology* 457: 38–46. https://doi.org/10.1016/j.chemgeo.2017.03.011.

Stewart, E. M., and J. J. Ague. 2020. "Pervasive Subduction Zone Devolatilization Recycles $CO_2$ Into the Forearc." *Nature Communications* 11: 1–8. https://doi.org/10.1038/s41467-020-19993-2.

Strating, E. H. H., and R. L. M. Vissers. 1991. "Dehydration-Induced Fracturing of Eclogite-Facies Peridotites: Implications for the Mechanical Behaviour of Subducting Oceanic Lithosphere." *Tectonophysics* 200: 187–198. https://doi.org/10.1016/0040-1951(91)90014-J.

Sun, Q., L. Xue, and S. Zhu. 2015. "Permeability Evolution and Rock Brittle Failure." *Acta Geophysica* 63: 978–999. https://doi.org/10.1515/acgeo-2015-0017.

Taetz, S., T. John, M. Bröcker, C. Spandler, and A. Stracke. 2018. "Fast Intraslab Fluid-Flow Events Linked to Pulses of High Pore Fluid Pressure at the Subducted Plate Interface." *Earth and Planetary Science Letters* 482: 33–43. https://doi.org/10.1016/j.epsl.2017.10.044.

Tajčmanová, L., J. Vrijmoed, and E. Moulas. 2015. "Grain-Scale Pressure Variations in Metamorphic Rocks: Implications for the Interpretation of Petrographic Observations." *Lithos* 216-217: 338–351. https://doi.org/10.1016/j.lithos.2015.01.006.

Tarling, M. S., S. A. F. Smith, and J. M. Scott. 2019. "Fluid Overpressure From Chemical Reactions in Serpentinite Within the Source Region of Deep Episodic Tremor." *Nature Geoscience* 12: 1034–1042. https://doi.org/10.1038/s41561-019-0470-z.

Trommsdorff, V., V. López Sánchez-Vizcaíno, M. T. Gómez-Pugnaire, and O. Müntener. 1998. "High Pressure Breakdown of Antigorite to Spinifex-Textured Olivine and Orthopyroxene, SE Spain." *Contributions to Mineralogy and Petrology* 132: 139–148. https://doi.org/10.1007/s004100050412.

Ulrich, M., D. Rubatto, J. Hermann, T. A. Markmann, A. Bouvier, and E. Deloule. 2024. "Olivine Formation Processes and Fluid Pathways in Subducted Serpentinites Revealed by In-Situ Oxygen Isotope Analysis (Zermatt-Saas, Switzerland)." *Chemical Geology* 649: 121978. https://doi.org/10.1016/j.chemgeo.2024.121978.

van Keken, P. E., B. R. Hacker, E. M. Syracuse, and G. A. Abers. 2011. "Subduction Factory: 4. Depth-Dependent Flux of $H_2O$ From Subducting Slabs Worldwide." *Journal of Geophysical Research* 116: B01401. https://doi.org/10.1029/2010JB007922.

Veveakis, E., S. Alevizos, and T. Poulet. 2017. "Episodic Tremor and Slip (ETS) as a Chaotic Multiphysics Spring." *Physics of the Earth and Planetary Interiors* 264: 20–34. https://doi.org/10.1016/j.pepi.2016.10.002.

Vho, A., P. Lanari, and D. Rubatto. 2019. "An Internally-Consistent Database for Oxygen Isotope Fractionation Between Minerals." *Journal of Petrology* 60: 2101–2129. https://doi.org/10.1093/petrology/egaa001.

Vho, A., P. Lanari, D. Rubatto, and J. Hermann. 2020. "Tracing Fluid Transfers in Subduction Zones: An Integrated Thermodynamic and $\delta^{18}O$ Fractionation Modelling Approach." *Solid Earth* 11: 307–328. https://doi.org/10.5194/se-11-307-2020.

Viete, D. R., B. R. Hacker, M. B. Allen, et al. 2018. "Metamorphic Records of Multiple Seismic Cycles During Subduction." *Science Advances* 4: 1–13. https://doi.org/10.1126/sciadv.aaq0234.

Wang, H., R. S. Huismans, and S. Rondenay. 2019. "Water Migration in the Subduction Mantle Wedge: A Two-Phase Flow Approach." *Journal of Geophysical Research - Solid Earth* 124: 9208–9225. https://doi.org/10.1029/2018JB017097.

Wark, D. A., C. A. Williams, E. B. Watson, and J. D. Price. 2003. "Reassessment of Pore Shapes in Microstructurally Equilibrated Rocks, With Implications for Permeability of the Upper Mantle." *Journal of Geophysical Research* 108: 2050. https://doi.org/10.1029/2001JB001575.

Warr, L. N. 2021. "IMA–CNMNC Approved Mineral Symbols." *Mineralogical Magazine* 85: 291–320. https://doi.org/10.1180/mgm.2021.43.

Warren-Smith, E., B. Fry, L. Wallace, et al. 2019. "Episodic Stress and Fluid Pressure Cycling in Subducting Oceanic Crust During Slow Slip." *Nature Geoscience* 12: 475–481. https://doi.org/10.1038/s41561-019-0367-x.

Waters, D. J., and D. P. Lovegrove. 2002. "Assessing the Extent of Disequilibrium and Overstepping of Prograde Metamorphic Reactions in Metapelites From the Bushveld Complex Aureole, South Africa." *Journal of Metamorphic Geology* 20: 135–149. https://doi.org/10.1046/j.0263-4929.2001.00350.x.

Wheeler, J. A. 2020. "Unifying Basis for the Interplay of Stress and Chemical Processes in the Earth: Support From Diverse Experiments." *Contributions to Mineralogy and Petrology* 175: 116. https://doi.org/10.1007/s00410-020-01750-9.

Wilson, C. R., M. Spiegelman, P. E. van Keken, and B. R. Hacker. 2014. "Fluid Flow in Subduction Zones: The Role of Solid Rheology and Compaction Pressure." *Earth and Planetary Science Letters* 401: 261–274. https://doi.org/10.1016/j.epsl.2014.05.052.

Winter, J. D. 2014. *Principles of Igneous and Metamorphic Petrology*. Pearson Education.

Yamato, P., T. Duretz, and S. Angiboust. 2019. "Brittle/Ductile Deformation of Eclogites: Insights From Numerical Models." *Geochemistry, Geophysics, Geosystems* 20: 3116–3133. https://doi.org/10.1029/2019GC008249.

Yamato, P., T. Duretz, M. Baïsset, and C. Luisier. 2022. "Reaction-Induced Volume Change Triggers Brittle Failure at Eclogite Facies Conditions." *Earth and Planetary Science Letters* 584: 117520. https://doi.org/10.1016/j.epsl.2022.117520.

Yoshino, T., J. D. Price, D. A. Wark, and E. B. Watson. 2006. "Effect of Faceting on Pore Geometry in Texturally Equilibrated Rocks: Implications for Low Permeability at Low Porosity." *Contributions to Mineralogy and Petrology* 152: 169–186. https://doi.org/10.1007/s00410-006-0099-y.

Zack, T., and T. John. 2007. "An Evaluation of Reactive Fluid Flow and Trace Element Mobility in Subducting Slabs." *Chemical Geology* 239: 199–216. https://doi.org/10.1016/j.chemgeo.2006.10.020.

Zhan, Z. 2020. "Mechanisms and Implications of Deep Earthquakes." *Annual Review of Earth and Planetary Sciences* 48, no. 1: 147–174. https://doi.org/10.1146/annurev-earth-053018-060314.

## Supporting Information

Additional supporting information can be found online in the Supporting Information section. **Data S1:** Input parameters for the petrochemical modelling software. P1—Benchmark input (Vho et al. 2020 recalculation). P2—Basalt and serpentinites simulation including the mechanical model. P3—Input of bulk rock sensitivity test. **Data S2:** Model descriptions, mechanical properties, modelling results of Section 4.1 and additional figure of brittle failure and fluid extraction in the *P–T* space. **Data S3:** Modelling results of Section 5.1. **Data S4:** Thermodynamic databases (tc55.txt, tc55_SERP.txt).